eLife

Reviewed Preprint
v2 • September 2, 2025
Revised by authors

Reviewed Preprint
v1 • May 9, 2025

Biochemistry and Chemical Biology

Blue-shifted ancyromonad channelrhodopsins for multiplex optogenetics

Elena G Govorunova, Oleg A Sineshchekov, Hai Li, Yueyang Gou, Hongmei Chen, Shuyuan Yang, Yumei Wang, Stephen Mitchell, Alyssa Palmateer, Leonid S Brown, François St-Pierre, Mingshan Xue, John L Spudich

Center for Membrane Biology, Department of Biochemistry & Molecular Biology, The University of Texas Health Science Center at Houston McGovern Medical School, Houston, United States • Department of Neuroscience, Baylor College of Medicine, Houston, United States • The Cain Foundation Laboratories, Jan and Dan Duncan Neurological Research Institute at Texas Children's Hospital, Houston, United States • Department of Chemical and Biomolecular Engineering, Rice University, Houston, United States • Department of Physics and Biophysics Interdepartmental Group, University of Guelph, Guelph, Canada • Department of Biochemistry and Molecular Biology, Baylor College of Medicine, Houston, United States • Systems, Synthetic, and Physical Biology Program, Rice University, Houston, United States • Department of Electrical and Computer Engineering, Rice University, Houston, United States • Department of Molecular and Human Genetics, Baylor College of Medicine, Houston, United States

eLife Assessment

This **important** study describes newly identified light-gated ion channel homologs (channelrhodopsins, ChRs) in several protist species, with a primary focus on the biophysical characterization of ChRs of ancyromonads. The authors employed a powerful combination of bioinformatics, manual and automated patch-clamp electrophysiology, absorption spectroscopy, and flash photolysis. Additionally, they evaluated the applicability of the newly discovered anion-conducting ChRs in cortical neurons of mouse brain slices and in living C. elegans worms. The evidence supporting most of the claims is **compelling**, and this work will be of interest to the microbial rhodopsin community and neuro- and cardioscientists utilizing optogenetics in their research.

https://doi.org/10.7554/eLife.106508.2.sa4

Abstract

Light-gated ion channels from protists (channelrhodopsins or ChRs) are optogenetic tools widely used for controlling neurons and cardiomyocytes. Multiplex optogenetic applications require spectrally separated molecules, which are difficult to engineer without disrupting channel function. Scanning numerous sequence databases, we identified three naturally blue-shifted ChRs from ancyromonads. They form a separate branch on the phylogenetic tree and contain residue motifs characteristic of anion ChRs (ACRs). However, only two conduct chloride, whereas the closely related *Nutomonas longa* homolog generates inward cation

currents in mammalian cells under physiological conditions, significantly exceeding those by previously known tools with similar spectral maxima (peak absorption at ~440 nm). Measurements of transient absorption changes and pH titration of purified proteins combined with mutant analysis revealed the roles of the residues in the photoactive site. Ancyromonad ChRs could be activated by near-infrared two-photon illumination, a technique that enables the deeper-tissue optogenetic activation of specific neurons in three dimensions. Both ancyromonad ACRs allowed optogenetic silencing of mouse cortical neurons in brain slices. *Ancyromonas sigmoides* ACR (*Ans*ACR) expression in cholinergic neurons enabled photoinhibition of pharyngeal muscle contraction in live worms. Overall, our results deepen the mechanistic understanding of light-gated channel function and expand the optogenetic toolkit with potent, blue-shifted ChRs.

Impact statement

Ancyromonad channelrhodopsins advance our understanding of ionic selectivity and wavelength regulation in light-gated ion channels, and expand the toolkit for multiplexing with red-shifted fluorescent sensors.

Introduction

Channelrhodopsins (ChRs) are retinylidene proteins acting as photoreceptors that mediate photomotility in green flagellate algae (Sineshchekov, Jung et al. 2002) and are also found in other protist lineages. The chromophore is attached via a retinylidene Schiff base (RSB) linkage to a conserved lysine residue in the 7^{th} transmembrane helix (TM7). Upon photoexcitation, ChRs generate passive ionic currents across the cell membrane and are used for optical control of excitable animal cells (optogenetics) (Deisseroth 2021, Piatkevich and Boyden 2023). The seven-transmembrane (7TM) domain is sufficient for channel activity; the role of the C-terminal domain, which comprises up to half of the polypeptide chain, remains unclear. A considerable diversity within the ChR family suggests a convergent evolution of light-gated channel function (Govorunova, Sineshchekov et al. 2022). ChRs form dimers (Volkov, Kovalev et al. 2017, Li, Huang et al. 2019) or trimers (Tucker, Sridharan et al. 2022, Morizumi, Kim et al. 2023), but their ionic conductance is intrinsic to individual protomers, unlike voltage- or ligand-gated channels, in which several protomers contribute to the channel pore. Anion channelrhodopsins (ACRs) generate photoinduced anion influx in mammalian cells; cation channelrhodopsins (CCRs) generate H^+ and Na^+ influx; and kalium channelrhodopsins (KCRs) generate K^+ efflux (Govorunova, Sineshchekov et al. 2022, Govorunova, Sineshchekov et al. 2023). ACRs and KCRs are used for optogenetic neuronal inhibition, and CCRs are used for neuronal activation.

Increasingly popular all-optical electrophysiology, i.e., simultaneous perturbation and measurement of membrane potential using light-sensitive actuators and reporters, respectively, in the same genetically defined cells (Hochbaum, Zhao et al. 2014) requires spectrally non-overlapping optogenetic tools. Even the most red-shifted ChRs retain sufficient sensitivity to blue light due to their relatively wide spectral bandwidth (Oda, Vierock et al. 2018, Govorunova, Sineshchekov et al. 2020). The development of red-light-absorbing genetically encoded fluorescent biosensors for monitoring neural activity (Sakamoto and Yokoyama 2025) opened up the possibility of pairing them with blue-shifted ChRs. Molecular engineering yielded several blue-shifted ChRs (Kato, Kamiya et al. 2015), but mutagenetic perturbations of the binding pocket frequently harm channel function. A complementary approach is exploring natural ChR diversity to search for molecules with desired biophysical properties optimized by evolution. Approximately ~1,000 ChR sequences are currently known, but a much smaller number has been functionally characterized (Govorunova, Sineshchekov et al. 2022).

Here, we identified and characterized three ChR variants from bacterivorous ancyromonad flagellates. Ancyromonads (also known as planomonads) represent a distinct major clade near the most commonly inferred root of the eukaryote tree (Brown, Heiss et al. 2018). We conducted automated and manual patch clamp analyses of photocurrents upon expression of ancyromonad ChR cDNAs in cultured mammalian cells under one- and two-photon excitation and monitored transient light absorption changes using detergent-purified proteins. We show that two ancyromonad ChRs are anion-selective, while the third and most blue-shifted ChR conducts metal cations. We expressed ancyromonad ACRs in mouse cortical pyramidal neurons and demonstrated photoinhibition of action potentials in acute brain slices. The nematode *Caenorhabditis elegans* is an attractive model for analyzing nervous system function by optogenetic manipulation (Bergs, Henss et al. 2022). We used this model organism to demonstrate that a blue-shifted ancyromonad ACR enables efficient optogenetic inhibition of pharyngeal activity upon expression in the cholinergic neurons.

Results

Phylogeny, spectral sensitivity, and photon flux dependence

Our bioinformatic search identified ChR homologs in the ancyromonads *Ancyromonas sigmoides, Fabomonas tropica,* and *Nutomonas longa; Ancoracysta twista,* a predatory flagellate placed in the newly established supergroup Provora (Tikhonenkov, Mikhailov et al. 2022); the diatom *Odontella aurita*; and *Paraphysoderma sedebokerense*, a chytrid-like fungus from the phylum Blastocladiomycota. Phylogenetic analysis placed the ancyromonad ChRs on a separate branch of the ACR tree together with their metagenomic homologs from the TARA Oceans database (**Figure 1A**). The *A. twista* and *O. aurita* homologs clustered with known stramenopile ACRs. The *P. sedebokerense* sequence showed only a distant homology to previously known ACRs. **Figure 1 – figure supplement 1** shows a protein alignment of their 7TM domains compared with *Gt*ACR1, the best-characterized ACR from the cryptophyte *Guillardia theta* (Govorunova, Sineshchekov et al. 2015, Li, Huang et al. 2019). All these sequences exhibit a non-carboxylate residue at the primary counterion position, corresponding to Asp85 in TM3 of *Halobacterium salinarum* bacteriorhodopsin (BR), marked by the red arrow in **Figure 1 – figure supplement 1**, as found in all known ACRs. The 2nd carboxylate in the photoactive site, contributed by TM7 and corresponding to Asp212 of BR, is replaced with Glu in the *N. longa* sequence, and with Gln in the *P. sedebokerense* sequence (the blue arrow in **Figure 1 – figure supplement 1**).

We expressed cDNAs encoding the 7TM domains of seven homologs fused to a C-terminal mCherry tag in human embryonic kidney (HEK293) cells and recorded photocurrents using manual patch clamping. All three ancyromonad ChRs generated robust photocurrents and showed maximal sensitivity in the blue spectral range (**Figure 1B**). Based on their ionic selectivities (see the next section), we named the *A. sigmoides, F. tropica,* and *N. longa* homologs *Ans*ACR, *Ft*ACR, and *Nl*CCR, respectively. The spectral sensitivity of the *A. twista* and *O. aurita* homologs was in the blue-green range (**Figure 1 – figure supplement 2**, left). Partial replacement of Cl^- in the bath with non-permeable aspartate shifted reversal potential (Vr) to more positive values, confirming their anion selectivity (**Figure 1 – figure supplement 2**, middle and right). We named them *At*ACR, *Oa*ACR1, and *Oa*ACR2. However, their photocurrents were smaller than those of the ancyromonad homologs or exhibited strong desensitization (reduction of photocurrents during illumination), so we did not characterize them in more detail. No photocurrents were detected in cells transfected with the *P. sedebokerense* homolog, although its expression and membrane targeting were evident from the tag fluorescence. Therefore, we named this protein *Pars*R, where R means “rhodopsin”.

Next, we expressed the constructs encoding ancyromonad ChRs in *Pichia pastoris.* We purified the proteins using a mild detergent yielding 0.25, 0.35, and 0.15 mg purified protein per L culture for *Ans*ACR, *Ft*ACR, and *Nl*CCR, respectively. The absorption spectra of the purified proteins (**Figure**

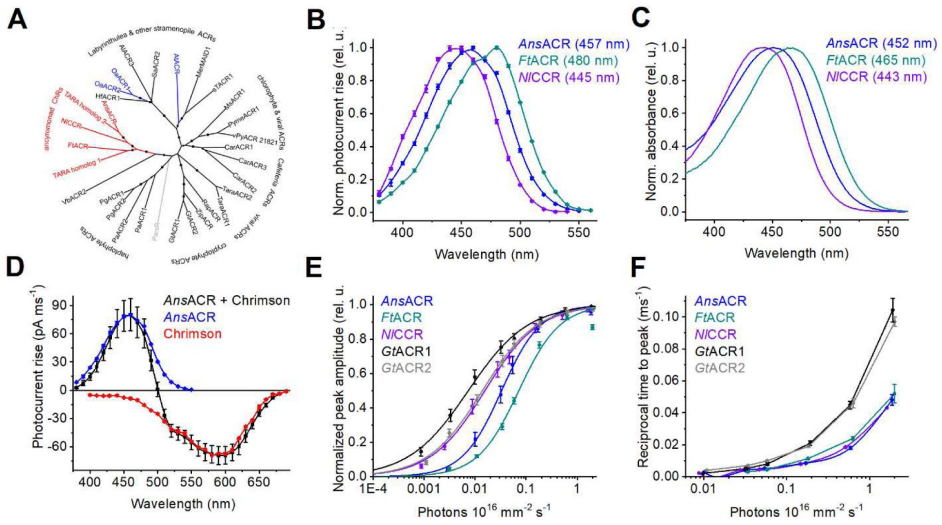

Figure 1.

Phylogeny, spectral sensitivity, and light dependence of ancyromonad ChRs.

(**A**) A maximum-likelihood phylogenetic tree of selected ChRs. The circles show bootstrap support from 40 to 100. (**B**) The photocurrent action spectra. The data points are the mean ± SEM values (n = 14 cells for *Ans*ACR, and 9 cells each for *Ft*ACR and *Nl*CCR). (**C**) The absorption spectra of detergent-purified proteins.
(**D**) The action spectra of photocurrents at −60 mV upon co-expression of *Ans*ACR and Chrimson, compared to each gene expressed alone. The data points are the mean ± SEM values (n = 14 cells each for the co-expression and *Ans*ACR, and 4 cells for Chrimson). (**E, F**) The dependence of the peak current amplitude (E) and reciprocal time to the peak (F) on the photon flux density for the indicated ChRs activated at their respective λmax. The data points are the mean ± SEM values (n = 8 cells for each variant).
The online version of this article includes the following source data for **Figure 1**:
Source data 1. Source data for the protein names and accession numbers used to construct the tree in (A); numerical values for the data shown in (B-F).

1C) were slightly blue-shifted from the respective photocurrent action spectra (**Figure 1 – figure supplement 3**), likely due to the presence of non-electrogenic *cis*-retinal-bound forms. The presence of such forms, explaining the discrepancy between the absorption and the action spectra, was verified by HPLC in KCRs (Tajima et al. 2023, Morizumi et al., 2025). To test the possibility of using *Ans*ACR in multiplex optogenetics, we co-expressed it with the red-shifted CCR Chrimson (Klapoetke et al., 2014) fused to an EYFP tag in HEK293 cells. We measured the action spectrum of the net photocurrents with 4 mM Cl^- in the pipette, matching the conditions in the neuronal cytoplasm (Doyon, Vinay et al. 2016). **Figure 1D**, black shows that the direction of photocurrents was hyperpolarizing upon illumination with λ<500 nm and depolarizing at longer wavelengths. A shoulder near 520 nm revealed a FRET contribution from EYFP (Govorunova, Sineshchekov et al. 2020), which was also observed upon expression of the Chrimson construct alone (**Figure 1D**, red). **Figures 1E and F** show the dependence of the peak photocurrent amplitude and reciprocal peak time, respectively, on the photon flux density for ancyromonad ChRs and *Gt*ACRs. The current amplitude saturated earlier than the time-to-peak for all tested ChRs. **Figure 1 – figure supplement 4A-E** shows normalized photocurrent traces recorded at different photon densities. Quantitation of desensitization at the end of 1-s illumination revealed a complex light dependence (**Figure 1, Figure Supplement 4F**). **Figure 1 – figure supplement 5** shows normalized photocurrent traces recorded in response to a 5-s light pulse of the maximal available intensity and the magnitude of desensitization at its end.

Characterization of ancyromonad ChRs by automated patch clamping

We used the fully automated planar patch clamp platform SyncroPatch 384 to characterize ancyromonad ChRs' photocurrents. This instrument uses KF-based internal and NaCl-based external solutions to promote gigaseal formation (Supplementary File 1). **Figure 2A-C** shows photocurrent traces evoked by 200-ms light pulses. The SyncroPatch enables unbiased estimation of the photocurrent amplitude because the cells are drawn into the wells without considering their tag fluorescence, unlike manual patch clamp studies in which the experimenter selects the fluorescent cells. **Figure 2 – figure supplement 1A, B** shows that the mean *Ans*ACR photocurrent measured by the SyncroPatch was significantly larger than the mean *Ft*ACR photocurrent, and the mean *Nl*CCR photocurrent was significantly larger than that of *Platymonas subcordiformis* channelrhodopsin 2 (*Ps*ChR2), a previously known excitatory optogenetic tool with a similar blue-shifted spectrum (Govorunova, Sineshchekov et al. 2013, Chen, Duan et al. 2022).

The voltage dependencies of photocurrents (IV curves) are shown in **Figure 2D-F**. *Ans*ACR and *Ft*ACR showed similarly negative Vr values, suggesting higher relative permeability to Cl^- than F-, as earlier found in *Gt*ACRs by manual patch clamping (Govorunova, Sineshchekov et al. 2015). The Vr values of the peak current and that at the end of illumination were not significantly different by the two-tailed Wilcoxon signed-rank test (**Fig. 2G**), indicating no change in the relative permeability during illumination. Unexpectedly, the *Nl*CCR photocurrents reversed near 0 mV (**Fig. 2F, G**). One reason for this behavior could be equal permeabilities of this ChR to Cl^- and F^-. However, when Cl^- in the external solution was partially replaced with bulky, non-permeable aspartate, only *Ans*ACR and *Ft*ACR showed substantial Vr shifts to more positive values, which confirmed their permeability to Cl^-, but no such shift was detected in *Nl*CCR (**Figure 2H-J**, red symbols). Control experiments conducted by manual patch clamping with the Cl^--based pipette solution confirmed these observations (**Figure 2 – figure supplement 2**). Upon replacing Cl^- with $NO3^-$, *Ans*ACR and *Ft*ACR, but not *Nl*CCR, showed Vr shifts to more negative values (**Figure 2H-J**, green), as did *Gt*ACRs examined by manual patch clamping (Govorunova, Sineshchekov et al. 2015), which indicated higher relative permeability to $NO3^-$ than to Cl^-. *Ft*ACR exhibited a larger Vr shift in $NO3^-$ than *Ans*ACR (p = 2.6E10-5 by the two-tailed Mann-Whitney test). Replacing Na^+ with N-methyl-D-gluconate ($NMDG^+$) resulted in a negative Vr shift in *Nl*CCR but not the other tested variants (**Figure 2H-J**, blue), suggesting that *Nl*CCR is permeable to Na^+. **Figure 2 – figure**

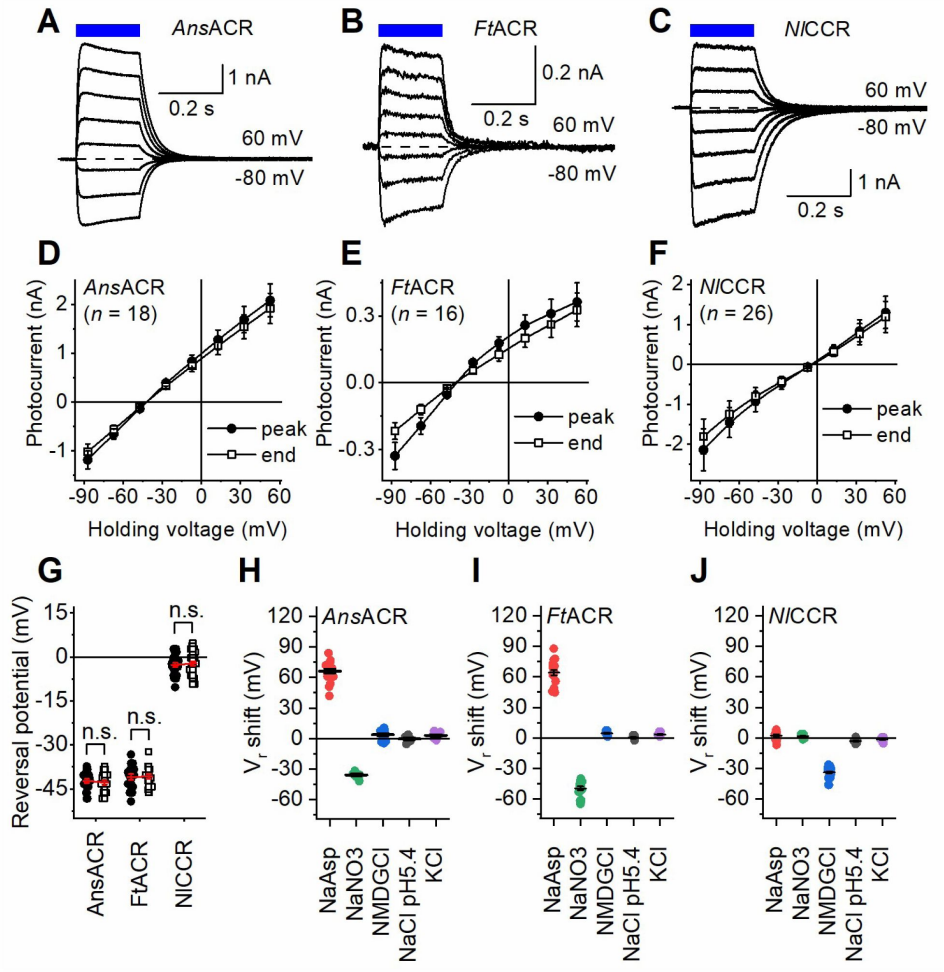

Figure 2.

Characterization of ancyromonad ChRs by automated patch clamping.

(**A-C**) Photocurrent traces recorded in response to 200-ms light pulses (470 nm) at voltages varied in 20-mV steps from −80 mV using the KF-based internal and NaCl-based external solutions. The dashed lines show the zero-current level. (**D-F**) The IV curves of the peak photocurrent (filled circles) and the current at the end of illumination (empty circles). The numbers in the parentheses are the numbers of cells sampled. (**G**) Comparison of the Vr at the photocurrent peak time (filled circles) and the end of illumination (empty circles). The p-values were determined by the two-tailed Wilcoxon signed-rank test; the number of cells sampled for each variant was the same as in panels D-F. (**H-J**) The Vr values in the indicated external solutions. The circles are the data from individual cells; the lines are the mean and SEM values.

The online version of this article includes the following source data for **Figure 2**:

Source data 1. Source data for the numbers of cells sampled and numerical values shown in (D-J).

supplement 1C, D compares *Nl*CCR with the typical cation-selective *C. reinhardtii* channelrhodopsin 2 (*Cr*ChR2), assessed using the same assay. Acidifying the external solution to pH 5.4 or replacing Na^+ with K^+ did not affect the Vr of any ancyromonad ChR (**Figure 2**, grey and violet). We conclude that only *Ans*ACR and *Ft*ACR are anion-selective, but *Nl*CCR conducts monovalent metal cations despite its sequence homology to the other two variants.

Channel gating and photochemical transitions under single-turnover conditions

Photocurrents evoked by continuous light pulses do not accurately reflect channel kinetics because different ChR molecules absorb photons at different times. Further complications result from photon absorption by photocycle intermediates. We conducted manual patch clamp recordings upon 6-ns laser flash excitation to analyze channel gating. *Ans*ACR and *Ft*ACR photocurrents exhibited biphasic rise and decay (**Figure 3A**, D), as the earlier characterized *Gt*ACR1 (Sineshchekov, Govorunova et al. 2015). The IV curves of all kinetic components revealed the same Vr values (**Figure 3 – figure supplement 1A, B**), meaning no ion selectivity changes occur during the single-turnover photocycle. Next, we analyzed transient absorption changes in detergent-purified *Ans*ACR and *Ft*ACR. In contrast to *Gt*ACR1, we could not find a clear indication of the accumulation of a blue-shifted L intermediate. After an initial (unresolved) decay of a K-like intermediate, red-shifted absorbance temporally increased in both ancyromonad ACRs, reaching a maximum at 100-200 μs (**Figure 3B, E**, red), i.e., in the time domain of fast channel opening. This red-shifted intermediate could be a long-lived K or an unusual red-shifted L. In *Ft*ACR, an additional slower increase in the red-shifted absorbance likely reflected the formation of an O-like intermediate (**Fig. 3E**, red). Accumulation of the M intermediate absorbing in the UV range was only 10 (*Ans*ACR) or 2 times (*Ft*ACR) slower than channel opening (**Figure 3C, F**), although in *Gt*ACR1 it was 50 times slower (Sineshchekov, Govorunova et al. 2015). Also, in contrast to prior observations in *Gt*ACR1, no temporal correlation was found between M formation and fast channel closing and between M decay and slow channel closing in ancyromonad ACRs. *Nl*CCR, the most blue-shifted among the ancyromonad ChRs we identified, has negligible absorption at 532 nm, the excitation laser's wavelength; therefore, its photochemical conversions could not be probed with our flash photolysis setup. In contrast to *Ans*ACR and *Ft*ACR, *Nl*CCR's laser-flash-induced photocurrent kinetics showed single exponential opening and closing in Cl^- and did not change upon its substitution with Asp^- in the bath solution (**Figure 3 – figure supplement 1C,D**).

While all ACRs have a non-carboxylate residue homologous to Asp85 in BR, the second counterion homologous to Asp212 in BR remains protonatable (**Figure 1 – figure supplement 1**, red arrow). To estimate the pKa of this counterion, we performed pH-titration of the absorption spectra (**Fig. 4A-C**). The titration curves revealed two transitions in all ancyromonad ChRs. Acidification caused a transition to longer peak absorption wavelengths, as expected upon protonation of the counterion, with pKa1s ~3.9, 2, and 3.4 for *Ans*ACR, *Ft*ACR, and *Nl*CCR, respectively. The maximum amplitude of this transition in *Ans*ACR (~8 nm) exactly corresponded to the 8-nm red shift of the photocurrent action spectrum in the *Ans*ACR_D226N mutant (**Fig. 4D**). The D226N mutation did not suppress photocurrent, but simplified its kinetics (**Fig. 4E**). Instead of the biphasic opening and closing observed in the WT, only two exponentials were sufficient to fit the D226N mutant's current, one for opening and one for closing. This observation suggested the role of Asp226 in channel gating, which was confirmed by analysis of the voltage dependence of the closing τ (**Fig. 4F**). Upon shifting to positive voltages, both components of channel closing accelerated in the WT, but the single-exponential closing slowed in the mutant, which suggests that oppositely directed charge movements control channel closing in the WT and the mutant.

Further acidification caused a transition to shorter wavelengths with similar pKa2s in both purified ancyromonad ACRs and only a slightly lower pKa2 in *Nl*CCR (**Fig. 4A-C**). It most probably reflects binding Cl^- in the photoactive site, as in archaeal rhodopsins (Shimono, Kitami et

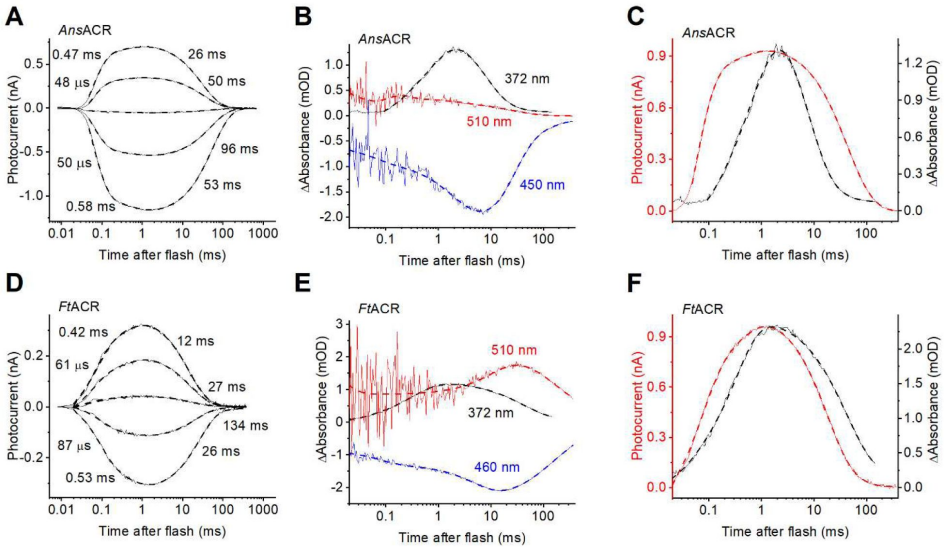

Figure 3.

Photocurrent and transient absorption changes under single-turnover conditions in *Ans*ACR and *Ft*ACR.

(**A, D**) Photocurrent traces of *Ans*ACR (A) and *Ft*ACR (D) evoked by 6-ns laser flashes recorded by manual patch clamping at the holding voltages increased in 30-mV steps from −60 mV. (**B, E**) Transient absorption changes recorded at the indicated wavelengths from detergent-purified proteins. (**C, F**) Comparison of the photocurrent kinetics (red, left axis) and the M intermediate kinetics (black, left axis). In all panels, the thin, solid lines are experimental recordings, and the thick, dashed lines are multiexponential approximations. The numbers are the τ values of the individual kinetic components.

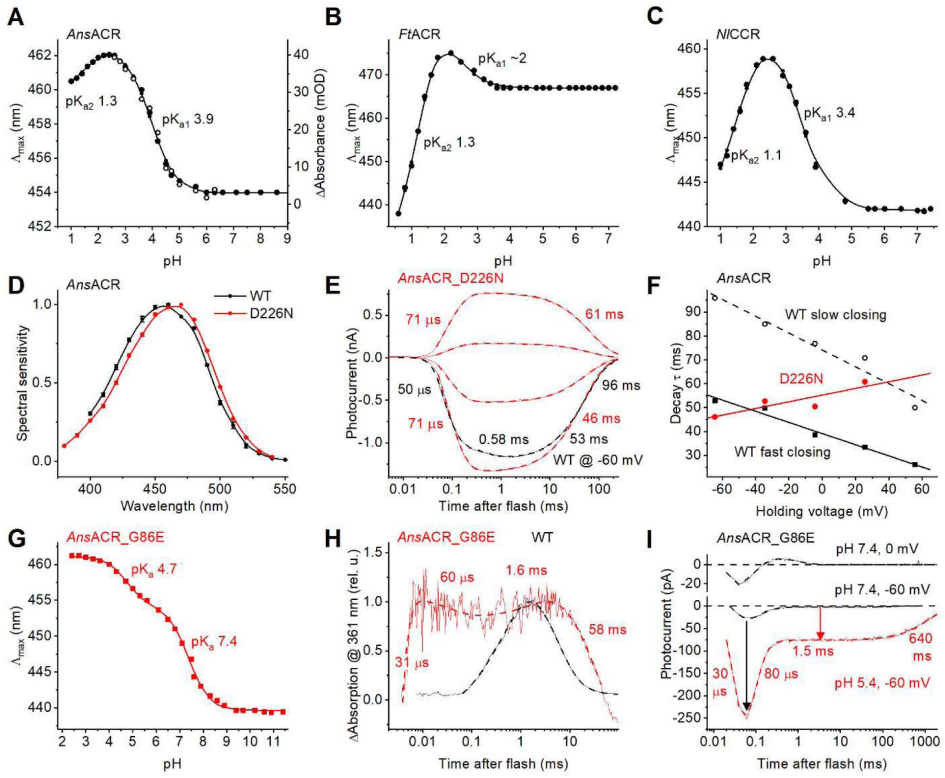

Figure 4.

Probing the residues in the counterion positions.

(**A**) pH titration of λmax (black filled circles, left axis) and maximal absorption changes (black empty circles, right axis) in wild-type *Ans*ACR. (**B, C**) pH titration of λmax in *Ft*ACR (B) and *Nl*CCR (C). (**D**) The photocurrent action spectrum of the *Ans*ACR_D226N mutant (red) compared to the WT (black). The data points are the mean ± SEM values (n = 8 cells). (**E**) Photocurrent traces of *Ans*ACR_D226N mutant evoked by 6-ns laser flashes recorded by manual patch clamping at the holding voltages increased in 30-mV steps from −60 mV. The wild-type photocurrent trace recorded at −60 mV is shown in black for comparison. The thin lines are experimental recordings, and the thick dashed lines are multiexponential approximations. The numbers are the τ values of the individual kinetic components. (**F**) The voltage dependence of the decay components τ in the *Ans*ACR_D226N mutant (red) and the WT (black). (**G**) pH titration of λmax in *Ans*ACR_G86E mutant. (**H**) Transient absorption changes monitored at the wavelength of the M intermediate absorption in the *Ans*ACR_G86E mutant (red) compared to the WT (black). (**I**) Laser-flash-induced photocurrents of the *Ans*ACR_G86E mutant recorded at the external pH 7.4 (black) and 5.4 (red). The arrow shows the increase in the channel current upon acidification.

The online version of this article includes the following source data for **Figure 4**:

Source data 1. Source data for the numerical values shown in (A-D, F, and G).

al. 2000). On the other hand, in contrast to *Natronomonas pharaonis* halorhodopsin (Váró, Brown et al. 1996), no blue spectral shift was detected in detergent-purified *Ans*ACR at neutral pH upon an increase in the Cl^- concentration (**Figure 4 – figure supplement 1**), which argued against Cl^- binding in the RSB region under these conditions.

Mutagenetic introduction of Glu in *Ans*ACR in the position of the primary acceptor in BR (the G86E mutation) led to the appearance of an additional spectral transition with pKa 7.4 upon pH titration of purified protein (**Fig. 4G**). An extremely fast M-like UV-absorbing intermediate absent in the WT was observed in the mutant (**Fig. 4H**, red). Its rise and decay τ corresponded to the rise and decay τ of the fast positive current recorded from *Ans*ACR_G86E at 0 mV and neutral pH, superimposed on the fast negative current reflecting the chromophore isomerization (**Figure 4I**, upper black trace). We interpret this positive current as an intramolecular proton transfer to the mutagenetically introduced primary acceptor (Glu86), which was suppressed by negative voltage (**Figure 4I**, lower black trace). Acidification increased the amplitude of the fast negative current ~10-fold (**Figure 4I**, black arrow) and shifted its Vr ~100 mV to more depolarized values (**Figure 4 – figure supplement 2A**). This can be explained by passive inward movement of the RSB proton along the large electrochemical gradient. Remarkably, the G86E mutation suppressed channel current at neutral pH, but acidification of the bath to pH 5.4 recovered it (**Figure 4I**, red arrow). The full current trace recorded under acidic conditions could be deconvoluted into four components with τ 30 μs, 80 μs, 1.5 ms, and 640 ms, revealing that the mutation slowed channel closing 6-fold. Replacement of Cl^- with Asp^- caused a ~40-mV shift of the channel current's Vr (**Figure 4 – figure supplement 2B**), indicating that the mutant channel remained Cl^- selective. These results confirm that the absence of a negative charge at the site corresponding to BR's primary acceptor is the ultimate condition for anion channel function.

Strong alkalization caused simultaneous depletion of absorption in the visible range, the appearance of the M-like states (at 368 nm in the wild-type *Ans*ACR and 355 nm in the *Ans*ACR_G86E mutant), and a substantial absorption increase at 297 nm, reflecting deprotonation of the RSB and a strong perturbation of the protein band (**Figure 4 – figure supplement 2C**). Analysis of the pH dependence of three parameters (absorption depletion in the visible range, absorption rise in the M-like states' range, and absorption rise at 297 nm) yielded similar pKa values, which were 11.1 and 10.7 for the WT and G86E, respectively (**Figure 4 – figure supplement 2D**). These high pKa values may explain the high photostability of this protein, as hundreds of laser flashes did not cause its measurable bleaching.

The glutamate in the middle of TM2 corresponding to Glu68 of *Gt*ACR1 is conserved in most ACRs, including *Ft*ACR, but is replaced with Gln in *Ans*ACR (**Figure 1 – figure supplement 1**, black arrow). Introducing the Q48E mutation in *Ans*ACR accelerated channel closing and slowed channel opening, making the photocurrent rise and decay monophasic (**Figure 4 – figure supplement 3A,B**).

The retinal-binding pocket and color tuning

The λmax of rhodopsins is regulated by the retinal chromophore geometry and steric and electrostatic interactions of the chromophore with amino acid residues of the retinal-binding pocket (Hoffmann, Wanko et al. 2006, Karasuyama, Inoue et al. 2018). Surprisingly, *Nl*CCR, the most blue-shifted among ancyromonad ChRs, features three residues typical of red-shifted microbial rhodopsins (**Figure 5A**). The first is Phe at the primary counterion position (Asp85 in BR), also found in RubyACRs from Labyrinthulea, the most red-shifted ChRs so far identified (Govorunova, Sineshchekov et al. 2020). The residues homologous to BR's Met118 near the β-ionone ring and Ala215 preceding the RSB lysine in the polypeptide chain are responsible for red-shifted absorption in many microbial rhodopsins (Shimono, Iwamoto et al. 2000, Engqvist, McIsaac et al. 2015, Oda, Vierock et al. 2018, Oppermann, Rozenberg et al. 2024) but are conserved in all three blue-absorbing ancyromonad ChRs. In *Gt*ACR1 (λmax 515 nm, (Govorunova, Sineshchekov et al. 2015, Sineshchekov, Li et al. 2016)), the only ACR with published atomic

structures (Kim, Kato et al. 2018, Li, Huang et al. 2019), the corresponding residues are Ser97, Cys133, and Cys237 (**Figure 5B**). As expected, the S97F, C133M, and C237A mutations red-shifted the *Gt*ACR1 spectrum (**Figure 5C**). The opposite F104S, M143C, and A242C mutations at the corresponding sites in the RubyACR from *Hondaea fermentalgiana* (*Hf*ACR1) caused large blue spectral shifts (**Figure 5D**). However, the corresponding mutations F85S, M141C, and A236C red-shifted the *Nl*CCR spectrum (**Figure 5E**). The same paradoxical behavior was observed upon mutation of the Met118 homolog to Val, which blue-shifted the *Hf*ACR1 spectrum but red-shifted the ancyromonad ChR spectra (**Figure 5F-H**). Replacement of the Ala215 homolog with Cys or Ser did not change the *Ans*ACR and *Ft*ACR spectra (**Figure 5 – figure supplement 1A, B**).

In blue-shifted ChRs such as *Ps*ChR2 (Govorunova, Sineshchekov et al. 2013) and *Klebsormidium nitens* channelrhodopsin (*Kn*ChR) (Tashiro, Sushmita et al. 2021), the position of BR's Met118 is occupied by Gly or Ala (**Figure 5A**), which, together with the Ala four residues downstream (BR's Gly122), rotates the β-ionone ring out of the plane of the polyene chain, shrinking the *p*-conjugation and blue-shifting the spectrum (Wang, Natsume et al. 2025). The Ala corresponding to BR's Gly122 is also found in *Ans*ACR and *Nl*CCR (**Figure 5A**), but the *Ans*ACR_M134A/G and *Nl*CCR_M141A/G mutations did not change the spectra, nor did the *Ft*ACR_M140G_V144A mutation (**Figure 5 – figure supplement 1A-C**). These observations suggest that the residue geometry and/or interactions in the retinal-binding pocket in ancyromonad ChRs differ from the earlier studied microbial rhodopsins.

The residue position corresponding to BR's Leu93 is the color switch between blue- and green-absorbing proteorhodopsins (BPRs and GPRs, (Man, Wang et al. 2003)). *Ans*ACR exhibits a Gln residue in this position, as do BPRs, but *Ft*ACR has Leu, as do GPRs, and *Nl*CCR has Met (**Figure 5A**). The *Ft*ACR_L96Q and *Nl*CCR_M93Q mutations blue-shifted the spectra 20 and 7 nm, respectively (**Figure 5I**, J), indicating that this residue position contributes to color tuning in ancyromonad ACRs. *Nl*CCR, the most blue-shifted among ancyromonad ChRs, differs from *Ans*ACR and *Ft*ACR at the positions corresponding to Ser89 and Glu233 (*Nl*CCR numbering), and from *Ft*ACR, also at the position of Pro235 (the corresponding residues in *Gt*ACR1 are Thr101, Asp234, and Leu236, **Figure 5A**). The S89T, E233D, and P235I mutations red-shifted the *Nl*CCR spectrum (**Figure 5K**), indicating that these three positions contribute to the blue shift of wild-type *Nl*CCR compared with *Ans*ACR and *Ft*ACR. However, the T90S mutation did not change the *Ans*ACR spectrum, and the D226E mutation and a combination of the two mutations caused red spectral shifts in *Ans*ACR (**Figure 5 – figure supplement 1D**). Supplementary File 2 contains the λ values of the half-maximal amplitude of the long-wavelength slope of the spectrum, which can be estimated more accurately from the action spectra than the λ of the maximum.

Two-photon excitation

Optical manipulation of neuronal activity in dense tissue commonly relies on two-photon (2P) excitation, which is based on the nearly simultaneous absorption of two infrared photons, equivalent to the absorption of one photon in the visible range (Emiliani, Entcheva et al. 2022). To determine the 2P activation range of *Ans*ACR, *Ft*ACR, and *Nl*CCR, we conducted raster scanning using a conventional 2P laser, varying the excitation wavelength between 800 and 1,080 nm (**Figure 6 – figure supplement 1**). All three ChRs generated detectable photocurrents with action spectra showing maximal responses at ~925 nm for *Ans*ACR, 945 nm for *Ft*ACR, and 890 nm for *Nl*CCR (**Figure 6A**). These wavelengths fall within the excitation range of common Ti:Sapphire lasers, which are widely used in neuroscience laboratories and can be tuned between ~700 nm and 1,020-1,300 nm. To assess desensitization, cells expressing *Ans*ACR, *Ft*ACR, or *Nl*CCR were illuminated at the respective peak wavelength of each ChR at 15 mW for 5 seconds. *Gt*ACR1 and *Gt*ACR2, previously used in 2P experiments (Forli, Vecchia et al. 2018, Mardinly, Oldenburg et al. 2018), were included for comparison. The normalized photocurrent traces recorded under these conditions are shown in **Figure 6B-F**. The absolute amplitudes of 2P photocurrents at the

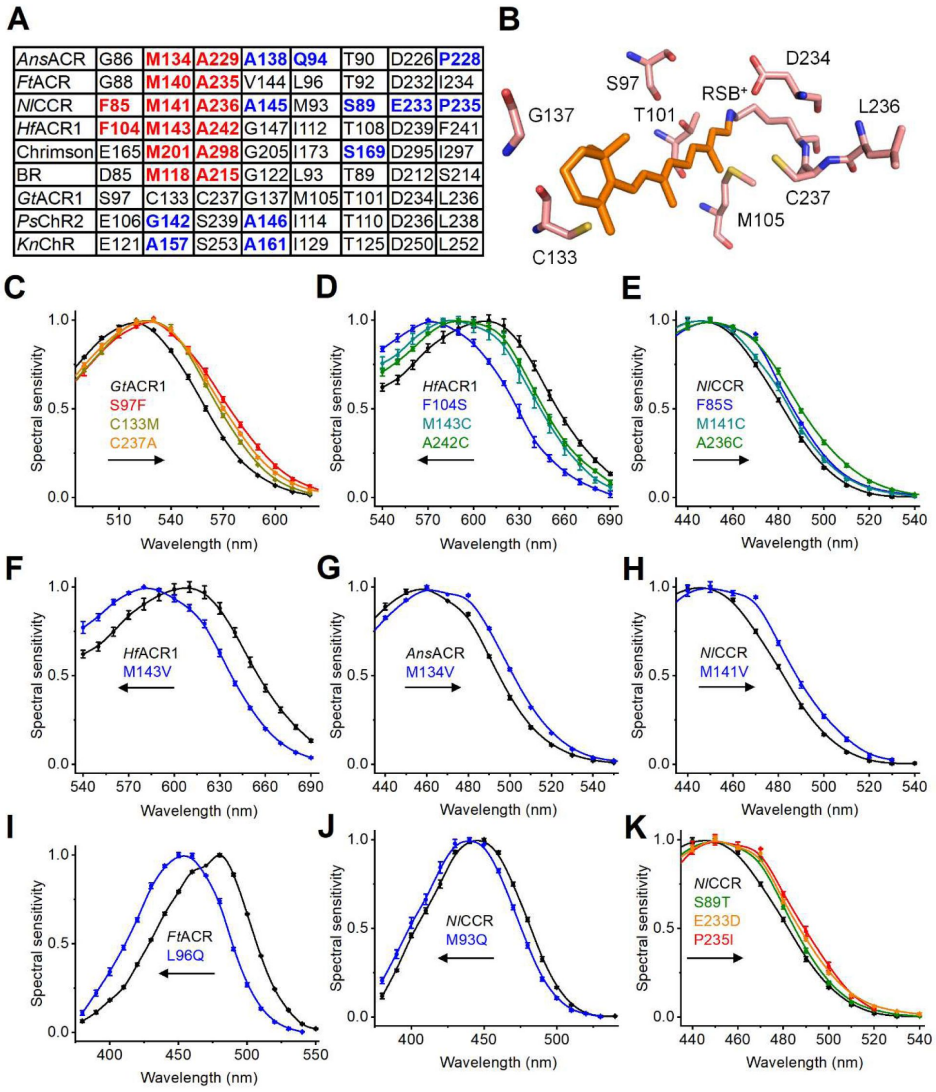

Figure 5.

Color tuning of ancyromonad ChRs.

(**A**) Amino acid residues of the retinal-binding pocket tested by mutagenesis in this study. (**B**) The corresponding residues in the *Gt*ACR1 structure (6edq). (**C-K**) The photocurrent action spectra of the indicated mutants compared to the respective WTs. The data points are the mean ± SEM values (the n values are provided in the Source Data 1).

The online version of this article includes the following source data for **Figure 5**:

Source data 1. Source data for the numbers of cells sampled and numerical values shown in (C-K).

peak time and at the end of illumination are shown in **Figure 6G and H**, respectively. All five tested variants exhibited comparable levels of desensitization at the end of illumination (**Figure 6I**).

Optogenetic inhibition of cortical neurons in mouse brain slices

To test the silencing efficiencies of *Ans*ACR and *Ft*ACR in mouse brain slices, we selectively expressed their 7TM domains fused with EYFP in the layer 2/3 pyramidal neurons of the somatosensory cortex by *in utero* electroporation at embryonic day 15. We prepared acute brain slices from 4-6-week-old mice and EYFP fluorescence was observed in the layer 1, layer 2/3 and layer 5, indicating clear *Ans*ACR-EYFP and *Ft*ACR-EYFP expression in dendrites, somata, and axons, respectively (**Figure 7 – figure supplement 1A**). We performed whole-cell current clamp recordings from *Ans*ACR- or *Ft*ACR-expressing neurons (for solution compositions, see Material and Methods). *Ans*ACR- and *Ft*ACR-expressing neurons showed the resting membrane potential, input resistance, and capacitance (**Figure 7 – figure supplement 1B**) similar to the typical values of untransfected cortical neurons (Xue, Atallah et al. 2014, Chen, Cai et al. 2020). When positive currents were injected into the somata to excite neurons, photoactivation of *Ans*ACR and *Ft*ACR suppressed the current-evoked action potentials, demonstrating the potency of these proteins as optogenetic silencers of mouse cortical neurons (**Figure 7**). We also observed that at rest or when a small negative current (e.g., −0.1 nA) was injected, the neurons could generate a single action potential at the beginning of photostimulation (**Figure 7A**, B), possibly caused by axonal depolarization, as reported in *Gt*ACR-expressing neurons (Mahn, Gibor et al. 2018, Messier, Chen et al. 2018).

Earlier studies have shown that photoactivation of *Gt*ACRs induces axonal depolarization and synaptic transmission in some ACR^+ neurons owing to the high intracellular Cl^- concentration at the axons (Mahn, Gibor et al. 2018, Messier, Chen et al. 2018). Indeed, when we recorded from ACR^- neurons in the electroporated cortical region, we found that photoactivation of either *Ans*ACR- or *Ft*ACR-induced excitatory post-synaptic currents (**Figure 7 – figure supplement 1C, D**), similar to other tested light-gated Cl^- channels.

Optogenetic inhibition of pharyngeal function in live C. elegans

To test *Ans*ACR as an optogenetic inhibitory tool in the context of an intact behaving animal, we expressed the encoding construct fused to a C-terminal EYFP tag in the *C. elegans* cholinergic neurons using the *unc-17* promoter (a scheme of the expression construct is shown in **Figure 8A**). C. *elegans* feeds on bacteria by rhythmic contractions and relaxations (pumping) of its pharynx. The cholinergic pharyngeal neurons, primarily MC neurons, entrain the pharyngeal muscle rhythm (Trojanowski, Raizen et al. 2016). Neuronal and muscular electrical activity leading to pharyngeal contractions can be monitored non-invasively by electropharyngeogram (EPG) recording (Raizen and Avery 1994). An EPG contains transients reflecting pharyngeal muscle action potentials (**Figure 8B**), the frequency of which can be easily quantified. In the presence of 10 mM serotonin required to maintain regular pharyngeal pumping, its frequency in the dark was not significantly different in the transgene and wild-type worms (4.07 ± 0.05 and 4.19 ± 0.08 Hz, respectively, mean ± SEM, n = 26 transgenic and 11 wild-type worms, respectively; the p-value by the two-tailed Mann-Whitney test is 0.21), indicating that *Ans*ACR expression did not affect the pharyngeal function in the darkness. **Figure 8C** shows representative EPG recordings from a transgenic worm fed on bacteria supplemented with all-*trans*-retinal. The onset of 470-nm illumination caused an immediate inhibition of pumping in such transgene worms but not in the WT worms fed on the same bacteria or transgene worms in the absence of retinal (**Figure 8D**). The *C. elegans* genome encodes LITE-1 and GUR-3 UV/blue light receptors (unrelated to ChRs) responsible for photoinhibition of pharyngeal pumping at high light levels (Bhatla, Droste et al. 2015). However, no photoinhibition was detected in the absence of retinal in either wild-type or transgenic worms. This indicates that the irradiance used in our experiments was insufficient to

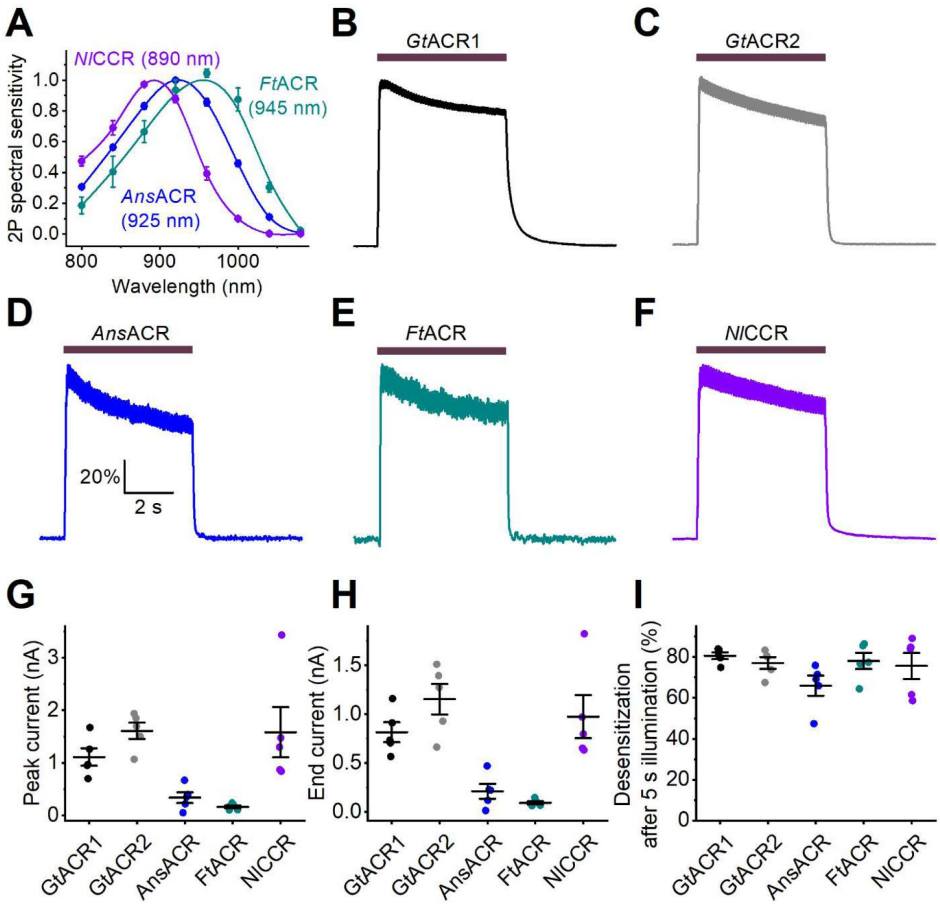

Figure 6.

2P excitation of ancyromonad ACRs.

(**A**) The 2P photocurrent action spectra. The data points are the mean ± SEM values (n = 5 cells for each variant). (**B-F**) The mean normalized photocurrent traces recorded upon 2P excitation from the indicated ChR variants (*Gt*ACR1 and *Gt*ACR2 are included for comparison) at +20 mV in the Cl^--based external solution (n = 6 cells for each variant). The illumination (the duration of which is shown as the bars on top) was 15 mW at the λmax for each variant. (**G, H**) The amplitude of photocurrent measured at the peak time (G) and at the end of 5-s illumination (H). (**I**) Desensitization at the end of illumination. In G-I, the symbols are the data from individual cells, the lines are mean ± SEM values (n = 6 cells for each variant). For more detail see Methods.

The online version of this article includes the following source data for **Figure 6**:

Source data 1. Source data for the numerical values shown in (A and G-I).

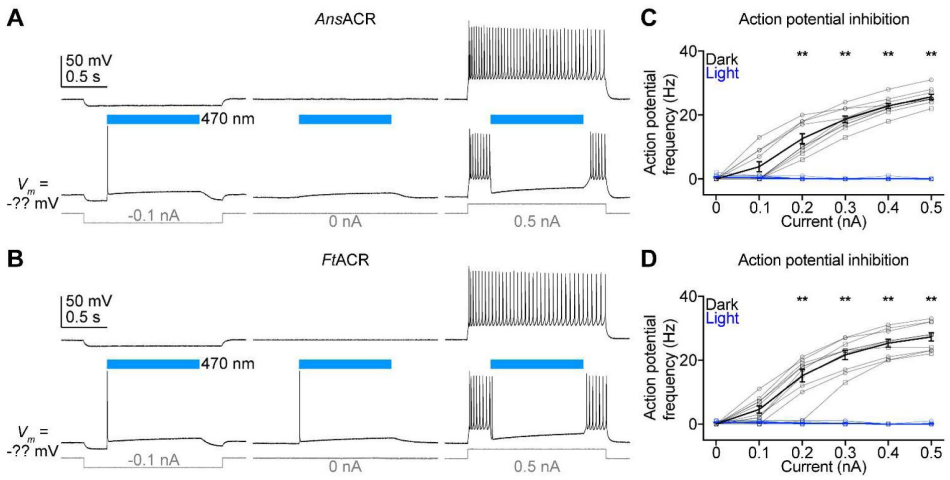

Figure 7.

Photoactivation of *Ans*ACR and *Ft*ACR inhibits the action potentials of mouse cortical neurons.

(**A, B**) Representative membrane voltage traces of neurons expressing *Ans*ACR (A) and *Ft*ACR (B) in response to −0.1 nA (left), 0 nA (middle), and 0.5 nA (right) injections without (top) and with (bottom) 470 nm light pulses (power density of 38.7 mW mm^{-2}). (**C, D**) The frequencies of action potentials evoked by different current injections with (blue) and without (black) photoactivation of *Ans*ACR (C) and *Ft*ACR (D). For all panels, data points from male mice are indicated by squares and female mice by circles. One male and one female mouse were used for each of the *Ans*ACR and *Ft*ACR experiments. Data are mean ± SEM.

**, p ≤ 0.01 for for comparison between dark and light stimulation at 0.2-0.5 nA current injection by the multiple Wilcoxon matched-pairs signed rank test with Benjamini, Krieger, and Yekutieli's corrections.

The online version of this article includes the following source data for **Figure 7**:

Source data 1. Source data for the numerical values shown in (C, D).

stimulate these endogenous photoreceptors. The magnitude of the *Ans*ACR-mediated photoinhibition depended on the irradiance (**Figure 8E**). The maximal irradiance (2.1 mW mm^{-2}) completely abolished the pumping for 15 s in all tested worms (n = 13). In five of 13 worms, individual action potentials were observed during the second half of the 30-s illumination period, an indication of adaptation. Two independently created transgenic lines showed the same degree of photoinhibition (**Figure 8E**, filled and empty symbols). The photoinhibition was fully reversible: after switching off the maximal-irradiance light, the pumping frequency returned to the pre-illumination level with τ ~9 s.

Discussion

ChRs, also known as "*Chlamydomonas* sensory rhodopsins," were first discovered as the photoreceptors guiding phototaxis and the photophobic response in the chlorophyte *C. reinhardtii* (Sineshchekov, Jung et al. 2002, Govorunova, Jung et al. 2004). Since then, ChRs have been identified in the genomes and transcriptomes of several other eukaryotic supergroups, including cryptophytes, haptophytes, stramenopiles, and alveolates (Govorunova, Sineshchekov et al. 2015, Govorunova, Sineshchekov et al. 2020, Govorunova, Sineshchekov et al. 2021). Furthermore, ChRs appear in the genomes of giant viruses, which likely facilitate the spread of ChR genes by horizontal transfer (Rozenberg, Oppermann et al. 2020, Zabelskii, Alekseev et al. 2020). Our identification and characterization of ChRs in ancyromonads, phylogenetically placed near the most commonly inferred root of the eukaryote tree (Brown, Heiss et al. 2018), suggests that eukaryotes acquired ChR genes at the early steps of their evolution. Consistent with the role of the encoded proteins as phototaxis receptors as shown in *C. reinhardtii*, ChR genes or transcripts have been found only in protists that develop flagella at some stage of their life cycle. The diatom *O. aurita*, in which we identified ChRs, is no exception: the flagella are lost in the vegetative state of this protist but are still present in its male gametes (Nanjappa, Sanges et al. 2017).

Prediction of biophysical properties such as ionic selectivity from protein sequences is a major unresolved problem in ChRs research. The *Nl*CCR sequence shows ~29% identity and ~49% similarity in the 7TM domain to each of the two ancyromonad ACRs and contains a neutral residue in the counterion position (Asp85 in BR), typical of all ACRs (**Figure 1 – figure supplement 1**, red arrow). Yet, *Nl*CCR does not conduct anions, showing instead permeability to Na^+. In the earlier known ChRs, the presence of conserved Glu residues in TM2 and the TM2-TM3 loop, corresponding to Glu82, Glu83, Glu90, and Glu101 of *Cr*ChR2, correlates with cation selectivity (Govorunova, Sineshchekov et al. 2021). However, TM2 of *Nl*CCR contains no carboxylated residues (**Figure 1 – figure supplement 1**), which suggests a unique mechanism of cation selection in this channel. *Nl*CCR is the most blue-shifted among ancyromonad ChRs and generates larger photocurrents than the earlier known *Ps*ChR2 with a similar absorption maximum (Govorunova, Sineshchekov et al. 2013), which makes *Nl*CCR a good candidate for optogenetic stimulation of neuronal activity with blue light.

All ancyromonad ChRs absorb light in the blue spectral range. The λmax of retinylidene proteins is determined by the energy gap between the electronic ground (S0) and first excited (S1) state of the chromophore and depend on the chromophore geometry, the protonation state of the Schiff base counterion, and the interaction of the chromophore with other residues of the retinal-binding pocket (Ernst, Lodowski et al. 2014, Engqvist, McIsaac et al. 2015, Kato, Kamiya et al. 2015). Paradoxically, the retinal-binding pockets of all three ancyromonad ChRs contain the residues corresponding to Met118 and Ala215 of bacteriorhodopsin, the well-known "color switches" characteristic of red-shifted microbial rhodopsins. The role of the near-ring Met118 homolog in red-shifting the spectrum has been experimentally verified in *Haloquadratum walsbyi* BR (Sudo, Okazaki et al. 2013), *Gloeobacter violaceus* rhodopsin (Engqvist, McIsaac et al. 2015), archaeorhodopsin-3 (Kato, Kamiya et al. 2015), and Chrimson (Oda, Vierock et al. 2018). It is

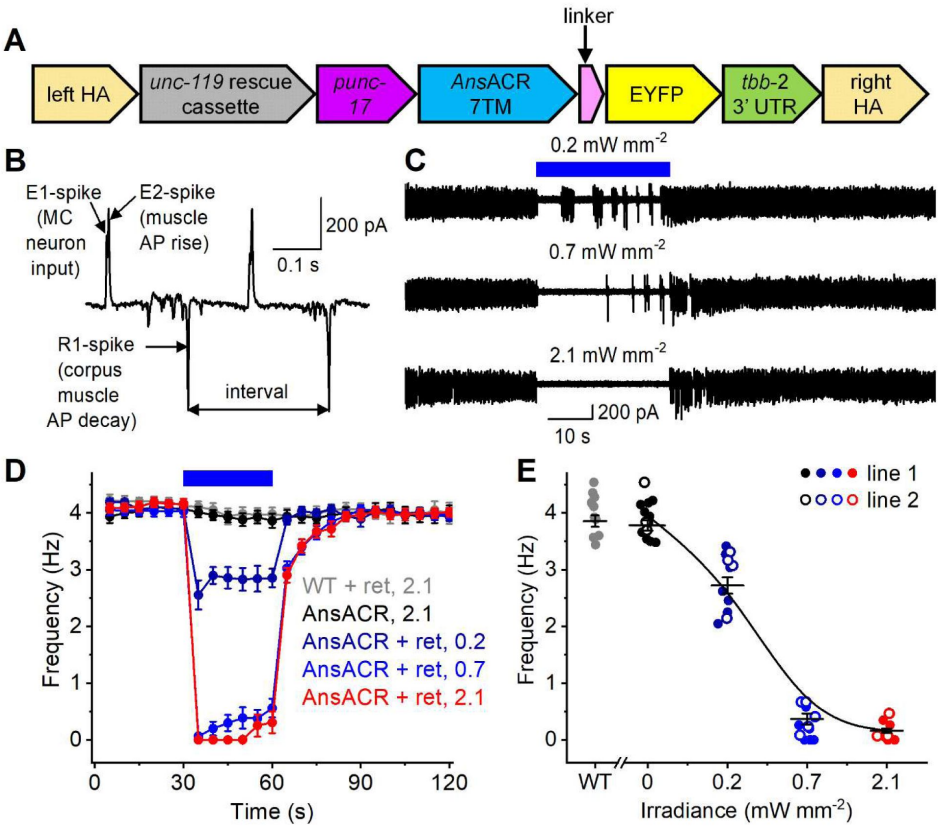

Figure 8.

Photoinhibition of pharyngeal pumping in live *C. elegans* expressing *Ans*ACR in the cholinergic neurons.

(**A**) A scheme of the genetic construct for *Ans*ACR expression in the cholinergic neurons. HA, homology arms. (**B**) A zoomed-in section of an EPG recording. AP, action potential; TB, terminal bulb. The double-headed arrow shows the interval between two successive R1 spikes used to calculate pharyngeal pumping frequency. (**C**) Electropharyngeogram recordings from an *Ans*ACR-expressing worm illuminated with 470 nm light at the indicated irradiances. The blue bar shows the duration of illumination. (**D**) The frequency of the pharyngeal pumping calculated from recordings as shown in A. The symbols are the mean values, and the error bars are the SEM values (n = 11 worms for the WT and 13 worms per condition for the transgenic worms). The numbers are the irradiance values in mW mm^{-2}; ret is retinal. (**E**) The dependence of the pharyngeal pumping frequency on the irradiance calculated from the 30-60 s segment of the data shown in B. The symbols are the data from individual worms; the lines are the mean and SEM values. The empty and filled symbols for the transgenic worms show the data from two independently created transgenic lines.

The online version of this article includes the following source data for **Figure 8**:

Source data 1. Source data for the numerical values shown in (D, E).

thought that the bulky Met side chain pushes away the C7 atom of retinal, increasing the ring-chain coplanarity, expanding the π-conjugation, and red-shifting absorbance, as theoretically predicted in the *Gt*ACR1_C133M mutant (Tsujimura, Noji et al. 2021). The red-shifting effect of the Ala215 homolog has been demonstrated in *N. pharaonis* sensory rhodopsin II (Shimono, Iwamoto et al. 2000), *H. salinarum* BR (Spudich, Ozorowski et al. 2012), Chrimson (Oda, Vierock et al. 2018), sodium-pumping rhodopsin KR2 (Inoue, Del Carmen Marin et al. 2019), and *Mantoniella squamata* ACR1 (Oppermann, Rozenberg et al. 2024), and is explained by electrostatic interactions between the polar residue in this position and the RSB. However, in ancyromonad ChRs, mutations of the Met118 homolog to smaller residues and the Ala215 homolog to polar residues caused a red spectral shift or no shift. Furthermore, the mutagenetic introduction of the ring-rotating residues responsible for the blue-shifted spectra of *Hyphochytrium catenoides* kalium channelrhodopsin 2 (*Hc*KCR2) (Tajima, Kim et al. 2023) and *Kn*ChR (Wang, Natsume et al. 2025) did not change the ancyromonad ChR spectra, which suggests that either the torsion around the C6-C7 bond is already enforced by a different geometry of the Met118 homolog or that the blue-shifted absorbance of ancyromonad ChRs arises by a different mechanism. Atomic structures of ancyromonad ChRs are needed to investigate the unexpected spectral shifts we observed when mutating residues of the retinal binding pocket.

ACRs are widely used to inhibit neuronal activity with light. We evaluated *Ans*ACR and *Ft*ACR as neuronal silencers in mouse brain slices and *Ans*ACR in the context of a live animal, the nematode *C. elegans*. We previously showed that *Gt*ACRs could inhibit action potentials at the soma while triggering synaptic transmission due to high axonal Cl^- reversal potential (Messier, Chen et al. 2018). *Ans*ACR and *Ft*ACR showed similar phenomena in our brain slice experiments. These ACRs can inhibit action potentials in cortical neurons but depolarize axonal terminals and trigger synaptic transmission at the onset of light stimulation. Fusing these new ACRs with somatodendritic trafficking motifs to reduce axonal expression (Mahn, Gibor et al. 2018, Messier, Chen et al. 2018) could lead to potent inhibition with reduced axonal excitation. Nevertheless, this undesired excitatory effect needs to be taken into consideration when using ACRs.

Optogenetic inhibition of *C. elegans* pharyngeal pumping has been demonstrated earlier upon expression of the *Leptosphaeria maculans* proton-pumping rhodopsin known as Mac (Trojanowski, Padovan-Merhar et al. 2014) or *N. pharaonis* halorhodopsin (*Np*HR) (Schuler, Fischer et al. 2015) in the cholinergic neurons. However, ion-pumping rhodopsins such as these transport only one ion per absorbed photon and, therefore, require almost 20 times higher irradiance for photoinhibition than the maximal irradiance used in this study. All ACRs, including *Ans*ACR that we tested in the worms, transport multiple anions during the open state and, therefore, are more efficient optogenetic silencers than the ion-pumping rhodopsins. One possible explanation of the partial recovery of pharyngeal pumping that we observed after 15-s illumination, even at the highest tested irradiance, is continued attenuation of photocurrent during prolonged illumination (desensitization). However, the rate of *Ans*ACR desensitization (**Figure 1 – figure supplement 4A** and **Figure 1 – figure supplement 5A**) is much faster than the rate of the pumping recovery, reducing the likelihood that desensitization is driving this phenomenon. Another possible reason for the observed adaptation is an increase in the cytoplasmic Cl^- concentration owing to *Ans*ACR activity and hence a breakdown of the Cl^- gradient on the neuronal membrane. The *C. elegans* pharynx is innervated by 20 neurons, 10 of which are cholinergic (Pereira, Kratsios et al. 2015). A pair of MC neurons is the most important for regulation of pharyngeal pumping, but other pharyngeal cholinergic neurons, including I1, M2, and M4, also play a role (Trojanowski, Padovan-Merhar et al. 2014). Moreover, the pharyngeal muscles generate autonomous contractions in the presence of acetylcholine tonically released from the pharyngeal neurons (Trojanowski, Raizen et al. 2016). Given this complexity, further elucidation of pharyngeal pumping adaptation mechanisms is beyond the scope of this study.

In summary, our characterization of ancyromonad channelrhodopsins (ChRs) reveals that their blue-shifted spectral sensitivity and unique ionic selectivity arise from distinct residue motifs not found in previously characterized ChRs. These findings broaden our understanding of how protein sequence modulates light-gated channel function. The blue-shifted absorption properties of ancyromonad ChRs hold promise for multiplexed applications alongside red-shifted indicators and warrant further evaluation across diverse experimental systems.

Materials and Methods

Bioinformatics and molecular biology

The ChR homologs from *Ancyromonas sigmoides* strain B-70 (CCAP1958/3), *Fabomonas tropica* strain NYK3C, *Nutomonas longa* strain CCAP 1958/5 (Torruella, de Mendoza et al. 2015, Brown, Heiss et al. 2018), and *Ancoracysta twista* strain TD-1 (Janouškovec, Tikhonenkov et al. 2017) were identified in the EukProt V3 database (Richter, Berney et al. 2022) using Sequnceserver BLASTP (Priyam, Woodcroft et al. 2019). The *A. sigmoides*, *F. tropica*, and *A. twista* ChR sequences are also available from Dr. Andrey Rozenberg's ChR database (Rozenberg 2024). The metagenomic homolog 1 was found by Sequnceserver BLASTP in the TARAeuCatV2 database (Sunagawa, Coelho et al. 2015) accessed at the KAUST Metagenomic Analysis Platform (KMAP) (Alam, Kamau et al. 2021). The metagenomic homolog 2 was found using the search mode of BLASTP in the MATOU database (Marine Atlas of Tara Oceans Unigene plus metaG eukaryotes) (Villar, Vannier et al. 2018) with the query sequence of *Nl*CCR. The *Odontella aurita* strain CCMP816 homologs GHBW01284417 and GHBW01118808 were identified by TBLASTN in the National Center of Biological Information (NCBI) transcriptome shotgun assembly (TSA) project GHBW00000000. The *Paraphysoderma* homolog (*Pars*R) was found in the *P. sedebokerense* strain JEL821 v. 1.0 genome assembly (Amses, Simmons et al. 2022) by the annotation text search using bacteriorhodopsin as a keyword at the Mycocosm portal (Ahrendt, Mondo et al. 2023).

The protein alignment was created using the MUSCLE algorithm with default parameters implemented in MegAlign Pro software v. 17.1.1 (DNASTAR Lasergene, Madison, WI) and truncated after the end of TM7. Phylogeny was analyzed with IQ-TREE v. 2.1.2 (Minh, Schmidt et al. 2020) using automatic model selection and ultrafast bootstrap approximation (1,000 replicates) (Hoang, Chernomor et al. 2018). The best tree was visualized and annotated using iTOL v. 7 (Letunic and Bork 2024). PyMol (v. 2.4.1, Schrödinger) was used for molecular visualization.

For expression in human embryonic kidney (HEK293) cells, mammalian codon-optimized polynucleotides encoding amino acid residues 1-265 of the *A. sigmoides* homolog, 1-268 of the *F. tropica* homolog, 1-272 of the *N. longa* coding homolog, 1-243 of the *A. twista* homolog, 1-241 of the GHBW01284417 *O. aurita* homolog, 1-242 of the GHBW01118808 *O. aurita* homolog, and 1-336 of the *P. sedebokerense* homolog were synthesized, fused to a C-terminal mCherry tag, and cloned into the pcDNA3.1(+) vector (Invitrogen, Cat. #V19520) at GenScript. Mammalian codon-optimized polynucleotides encoding amino acid residues 1-295 of *Gt*ACR1 (Genbank Acc. #KP171708), 1-291 of *Gt*ACR2 (Genbank Acc. #KP171709), and 1-350 of *Chlamydomonas noctigama* ChR1 known as Chrimson (Genbank Acc. #KF992060) were fused to a C-terminal EYFP (enhanced yellow fluorescent protein) tag and cloned into the same vector backbone. For expression in *Pichia*, the constructs were fused with the C-terminal 8His-tag and cloned in the pPICZalpha-A vector (Invitrogen, Cat. #V19520). A QuikChange XL site-directed mutagenesis kit (Agilent Technologies, Cat. #200516) was used to introduce point mutations. For expression in the mouse cortical neurons, *Ans*ACR and *Ft*ACR were tagged with EYFP at the C-terminus and cloned into the pAAV-CAG vector.

HEK293 cell culture and transfection

No cell lines from the list of known misidentified cell lines maintained by the International Cell Line Authentication Committee were used in this study. HEK293 cells used in one-photon (1P) excitation experiments were obtained from the American Type Culture Collection (ATCC, Cat. #CRL-1573). The cells were plated on 2-cm diameter plastic dishes 48-72 hrs before experiments, grown for 24 hrs, and transfected with 10 µl of Lipofectamine LTX with Plus Reagent (ThermoFisher, Cat. #15338100) using 3 µg DNA per dish for manual patch clamping, and 6 µg DNA per dish for automated patch clamping. All-*trans*-retinal (Millipore-Sigma, Cat. #116-31-4) was added immediately after transfection at the final concentration of 5 µM.

For 2P excitation experiments, HEK293A cells (Invitrogen, Cat. # R70507) were plated on 30-70 kDa poly-*d*-lysine-coated 12-mm circular coverslips (Carolina cover glass #0, Cat. #633009) in 24-well plates (P24-1.5H-N, Cellvis) at 30% confluence, transfected with 1.2 µL FuGENE HD transfection reagent (Promega, Cat. #E2311) using 200 ng DNA per well 48-72 h before measurements, and supplemented with all-*trans*-retinal as described above.

Automated whole-cell patch clamp recording from HEK293 cells

Automated patch clamp recording was conducted at room temperature (21°C) with a SyncroPatch 384 (Nanion Technologies) based on a Biomek i5 automated liquid handler (Beckman Coulter), using NPC-384T S-type chips (Nanion, Cat. #222101) with one hole per well, as described earlier (Govorunova, Sineshchekov et al. 2022). Transfected cells (48-72 h after transfection) were dissociated using TrypLE Express, diluted with CHO-S-SFM-II medium (both from ThermoFisher, Cat.# 12604013 and 31033020, respectively), and resuspended in External Physiological solution (Nation, Cat.# 08 3001). The compositions of this and other solutions used in automated patch clamp recordings and the corresponding liquid junction potential (LJP) values calculated using the ClampEx LJP calculator are listed in Supplementary File 1. The voltages in all IV curves for HEK293 cells studied under 1P excitation in this manuscript were corrected for LJPs; the holding voltage values in the figures showing traces correspond to the amplifier output before the LJP subtraction. Illumination was provided with LUXEON Z Color Line light-emitting diodes (LEDs) Cat.# LXZ1-PB01 (470 ± 10 nm) arranged in a 6×16 matrix. The forward LED current was 900 mA (which corresponded to the irradiance of ~2 mW mm^{-2}), the illumination duration was 200 ms (limited by the LED duty cycle), and the interval between successive light pulses was 60 s. The LEDs were driven by a derivative of CardioExcyte 96 SOL (Nanion, Cat. #191003) and controlled by Biomek commands. PatchControl384 v. 2.3.0 (Nanion Technologies) software was used for data acquisition at a 5 kHz sampling rate (200 µs per point). The photocurrent amplitudes at the peak and the end of illumination were calculated using DataControl384 software v. 2.3.0 (Nanion Technologies). Further analysis was performed using the Origin Pro 2016 software (OriginLab Corporation).

Manual patch clamp recording using 1P excitation in HEK293 cells

Manual patch clamp recordings were performed with an Axopatch 200B amplifier (Molecular Devices). The pipette solution contained (in mM) KCl 130, MgCl2 2, HEPES 10 pH 7.4, and the bath solution contained (in mM) NaCl 130, CaCl2 2, MgCl2 2, glucose 10, HEPES 10 pH 7.4. In experiments to test the relative permeability of ChRs for Cl^-, NaCl in the bath was replaced with Na aspartate, and in experiments in cells co-transfected with *Ans*ACR and Chrimson, KCl in the pipette solution was replaced with K gluconate. The low-pass filter of the amplifier output was set to 2 kHz. The signals were digitized with a Digidata 1440A (Molecular Devices) at a 250-kHz sampling rate (4 µs per point) in experiments with laser flashes, and at a 5-kHz sampling rate (200 µs per point) in experiments with continuous light pulses using pClamp 10.7. Patch pipettes with 2-3 MΩ resistances were fabricated from borosilicate glass. Laser excitation was provided by a Minilite Nd:YAG laser (532 nm, pulse width 6 ns, energy 5 mJ; Continuum). The current traces were logarithmically filtered using Logpro software (Spudich 2022). Curve fitting was performed

using Origin Pro software. Continuous light pulses were provided by a Polychrome V light source (T.I.L.L. Photonics GMBH) in combination with a mechanical shutter (Uniblitz Model LS6, Vincent Associates; half-opening time 0.5 ms). The action spectra of photocurrents were constructed by calculating the initial slope of photocurrent recorded in response to 15-ms light pulses at the intensity <25 μW mm^{-2}, corrected for the quantum density measured at each wavelength, and normalized to the maximal value. To analyze the dependence of photocurrents on the photon flux density, 1-s light pulses were applied with 60-s dark intervals starting from the lowest density. Calibrated neutral density filters (Newport, Cat. #FSQ-OD50, #FSQ-OD100, #FSQ-OD150, and #FSQ-OD200) were used to adjust the density.

Manual patch clamp recording using 2P excitation in HEK293A cells

2P excitation of *Ans*ACR, *Ft*ACR, *Nl*CCR, *Gt*ACR1, and *Gt*ACR2 expressed in HEK293A cells was conducted using an inverted microscope with multiphoton capability (A1R-MP, Nikon Instruments) at room temperature (23°C). A coverslip seeded with the transfected cells was placed in a custom glass-bottom chamber based on Chamlide EC (Live Cell Instrument) with a glass bottom made with a 24×24 mm cover glass #1 (Erie Scientific, Cat. #89082-270). Cells were perfused continuously with the external solution as described in the 1P excitation section. Whole-cell voltage-clamp recordings were performed using a MultiClamp 700B amplifier (Molecular Devices). Cells were held at −20 mV for power dependency and spectral measurements, and at +20 mV for desensitization measurements. The holding voltages were compensated for the 4.4 mV LJP calculated using the ClampEx v.11.1 (Molecular Devices) built-in calculator. The signals were digitized with an Axon Digidata 1550B1 Low Noise system with a HumSilencer (Molecular Devices), and the current was recorded at 10 kHz using pClamp. The near-IR excitation was generated by a titanium:sapphire femtosecond laser (Chameleon Ultra II, Coherent) with a repetition rate of 80 MHz and a tuning range between 680 and 1,080 nm. Laser pulses were not pre-compensated for dispersion in the microscope optical path. Laser power was tuned using an acousto-optic modulator and delivered to the sample plane through a 40×0.95-numerical aperture (NA) objective (CFI Plan Apochromat Lambda, Nikon Instruments). Scanning across 40.96×40.96 μm regions-of-interest was achieved using resonant scanning at 33.3 Hz.

To determine the 2P action spectra of *Ans*ACR, *Ft*ACR, and *Nl*CCR, the excitation wavelength was varied from 800 to 1,080 nm in 40-nm increments. At each wavelength, the laser power at the sample plane was adjusted to 7.5 mW for *Ans*ACR, 5 mW for *Ft*ACR, and 3 mW for *Nl*CCR, as measured using a microscope slide power sensor (S170C, Thorlabs). Excitation power levels were selected to elicit robust photocurrents while minimizing ChR desensitization, by operating at or near the quadratic regime, where doubling the excitation power results in an approximate fourfold increase in the initial photocurrent slope. Deviations from the target power level were kept below 10% and corrected by considering the quadratic dependence of photocurrents on power under 2P excitation. Illumination consisted of 30 consecutive raster scans (total duration ~1 s) over a 40.96×40.96 μm region (512×512 pixels), approximating the average size of a HEK293A cell. Scans were performed back-to-back without temporal gaps, except for the brief interval required for the laser to return to the starting scan position. To mitigate desensitization, we spaced illumination pulses ~54 s apart. We verified that the power ramp and spectral scan protocols caused a less than 20% reduction in the peak photocurrent, as measured at the beginning and end of each protocol using peak-wavelength light pulses at 7.5 mW for *Ans*ACR, 5 mW for *Ft*ACR, and 3 mW for *Nl*CCR. The 2P action spectra were constructed by measuring the initial linear slope of the photocurrent rise at each wavelength and plotted using Origin Pro 2016 software.

For desensitization experiments, cells expressing *Ans*ACR, *Ft*ACR, *Nl*CCR, *Gt*ACR1, and *Gt*ACR2 were illuminated near their respective peak wavelengths: *Ans*ACR (920 nm), *Ft*ACR (960 nm), *Nl*CCR (920 nm), *Gt*ACR1 (1040 nm), and *Gt*ACR2 (940 nm) at 15 mW for 5 s. Current traces were low-pass filtered at 100 Hz and, for presentation purposes, downsampled by substituting an average value for each 100 data points. The *Ft*ACR trace was additionally smoothed by the 5-point

Savitzky-Golay algorithm in Origin. Peak currents were quantified as the maximal currents over the 5-sec traces. End currents were calculated as the mean current over the final 0.1 s of the 5-sec photoactivation pulse.

Expression and purification of ancyromonad ACRs from Pichia pastoris

The plasmids carrying the expression constructs were linearized with Sac I and delivered into the *P. pastoris* strain SMD1168 (ThermoFisher, Cat. # C17500) by electroporation. A single colony resistant to 0.25 mg/ml zeocin (ThermoFisher, Cat. #R25001) was picked and inoculated into buffered complex glycerol medium, after which the cells were transferred to buffered complex methanol (0.5%) medium supplemented with 5 μM all-*trans*-retinal (Millipore-Sigma, Cat. #116-31-4) and grown at 30 °C with shaking at 230 rpm. After 24 h, the yellow-colored cells were harvested by centrifugation at 5000 g for 10 min, and the cell pellets were resuspended in 100 ml ice-cold buffer A (20 mM HEPES, pH 7.4, 150 mM NaCl, 1 mM EDTA, 5% glycerol) and lysed by either French press or bead beater. After centrifugation at low speed (5000 g for 10 min) to remove cell debris, membrane fractions were pelleted at 190,000 g for 1 h using a Ti45 Beckman rotor. The membranes were suspended in Buffer B (350 mM NaCl, 5% glycerol, 20 mM HEPES, pH 7.5) with 1 mM phenylmethylsulfonyl fluoride and solubilized with 1% n-dodecyl-β-D-maltoside (DDM; Anatrace, Cat. # D310) for 1 h at 4 °C with shaking. Undissolved content was removed after ultracentrifugation using a Ti45 rotor at 110,000 g for 1 h. The supernatant supplemented with 15 mM imidazole was incubated with nickel-nitrilotriacetic acid resin (Qiagen, Cat. # 30210) for 1 h with shaking at 4 °C. The resin was washed step-wise using 15 mM and 40 mM imidazole in Buffer B supplemented with 0.03% DDM. The protein was eluted with 400 mM imidazole and 0.03% DDM in buffer B. Protein fractions were pooled and concentrated using a 50 kDa MWCO Amicon Ultra Centrifugal Filter (Millipore-Sigma, Cat. # UFC9050), flash-frozen in liquid nitrogen and stored at −80 °C until use.

Absorption spectroscopy and flash photolysis

Absorption spectra of detergent-purified protein samples were recorded using a Cary 4000 spectrophotometer (Varian). Photoinduced absorption changes were measured with a laboratory-constructed crossbeam apparatus. Excitation flashes were provided by a Minilite II Nd:YAG laser (532 nm, pulse width 6 ns, energy 5 mJ; Continuum). Measuring light was from a 250-W incandescent tungsten lamp and a McPherson monochromator (model 272, Acton). Absorption changes were detected with a Hamamatsu Photonics photomultiplier tube (model R928) combined with a second monochromator of the same type. Signals were amplified by a low noise current amplifier (model SR445A; Stanford Research Systems) and digitized with a GaGe Octopus digitizer board (model CS8327, DynamicSignals LLC), with a maximal sampling rate of 50 MHz. Logarithmic data filtration was performed using the GageCon program (Sineshchekov, Govorunova et al. 2023).

Mice

All procedures to maintain and use mice were approved by the Institutional Animal Care and Use Committee at Baylor College of Medicine (protocol AN-6544). Mice were maintained on a 14 hr:10 hr light:dark cycle with regular mouse chow and water ad libitum. The temperature was maintained at 21– 25°C and humidity at 40-60%. Experiments were performed during the light cycle. Female ICR (CD-1) mice were purchased from Baylor College of Medicine Center for Comparative Medicine, and male C57BL6/J (JAX #000664) mice were obtained from Jackson Laboratory. Both male and female mice were used in the experiments.

In utero electroporation

Female ICR mice were crossed with male C57BL6/J mice to obtain timed pregnancies. *In utero* electroporation was used to deliver the transgenes (Xue, Atallah et al. 2014). To express *Ans*ACR or *Ft*ACR in the layer 2/3 pyramidal neurons of the somatosensory cortex, pAAV-CAG-*Ans*ACR-EYFP or pAAV-CAG-*Ft*ACR-EYFP (2.5 μg μl^{-1} final concentration) was mixed with pCAG-tdTomato (0.1 μg μl^{-1} final concentration) and Fast Green (Sigma-Aldrich, 0.01% final concentration) for injection. On embryonic day 15, pregnant mice were anesthetized, and a beveled glass micropipette (tip size 100-μm outer diameter, 50-μm inner diameter) was used to penetrate the uterus and the embryo skull to inject ~1.5 μl DNA solution into one lateral ventricle. Five pulses of current (voltage 39 V, duration 50 ms) were delivered at 1 Hz with a Tweezertrode (5-mm diameter) and a square-wave pulse generator (Gemini X2, BTX Harvard Bioscience). The electrode paddles were positioned in parallel with the brain's sagittal plane. The cathode contacted the side of the brain ipsilateral to the injected ventricle to target the somatosensory cortex. Transfected pups were identified by the transcranial fluorescence of tdTomato with an MZ10F stereomicroscope (Leica) 1 day after birth.

Brain slice electrophysiology and imaging

Mice were used at the age of 4-6 weeks for acute brain slice electrophysiology experiments. Mice were anesthetized by an intraperitoneal injection of a ketamine and xylazine mix (80 mg kg^{-1} and 16 mg kg^{-1}, respectively) and perfused transcardially with cold (0-4°C) slice cutting solution containing 80 mM NaCl, 2.5 mM KCl, 1.3 mM NaH2PO4, 26 mM NaHCO3, 4 mM MgCl2, 0.5 mM CaCl2, 20 mM *d*-glucose, 75 mM sucrose and 0.5 mM sodium ascorbate (315 mOsm l^{-1}, pH 7.4, saturated with 95% O2/5% CO2). Brains were removed and sectioned in the cutting solution with a VT1200S vibratome (Leica) to obtain 300 μm coronal slices. Slices were incubated in a custom-made interface holding chamber containing slice cutting solution saturated with 95% O2/5% CO2 at 34°C for 30 min and then at room temperature for 20 min to 10 h until they were transferred to the recording chamber. We performed recordings on submerged slices in artificial cerebrospinal fluid (ACSF) containing 119 mM NaCl, 2.5 mM KCl, 1.3 mM NaH2PO4, 26 mM NaHCO3, 1.3 mM MgCl2, 2.5 mM CaCl2, 20 mM *d*-glucose and 0.5 mM sodium ascorbate (305 mOsm l^{-1}, pH 7.4, saturated with 95% O2/5% CO2, perfused at 3 ml min^{-1}) at 30-32°C. For whole-cell recordings, a K^+-based pipette solution containing 142 mM K^+ gluconate, 10 mM HEPES, 1 mM EGTA, 2.5 mM MgCl2, 4 mM ATP-Mg, 0.3 mM GTP-Na, 10 mM Na2-phosphocreatine (295 mOsm l^{-1}, pH 7.35) was used. Membrane potentials reported in **Figure 7** and **Figure 7 – figure supplement 1** were not corrected for LJP, which was 12.5 mV as measured experimentally. Neurons were visualized with video-assisted IR differential interference contrast imaging, and fluorescent neurons were identified by epifluorescence imaging under a water immersion objective (×40, 0.8 NA) on an upright SliceScope Pro 1000 microscope (Scientifica) with an IR-1000 CCD camera (DAGE-MTI). Data were acquired at 10 kHz and low-pass filtered at 4 kHz with an Axon Multiclamp 700B amplifier and an Axon Digidata 1440 A Data Acquisition System under the control of Clampex 10.7 (Molecular Devices). Data were analyzed offline using Clampfit (Molecular Devices). For photostimulation, blue light was emitted from a collimated 470 nm light-emitting diode (LED; M470L3, Thorlabs) to stimulate *Ans*ACR-or *Ft*ACR-expressing neurons. The LEDs were driven by a LED driver (Throlabs LEDD1B) under the control of an Axon Digidata 1440 A Data Acquisition System and Clampex 10.7. The light was delivered through the reflected light fluorescence illuminator port and the ×40 objective.

To evaluate the inhibition efficiency, action potentials of *Ans*ACR-or *Ft*ACR-expressing neurons were evoked by injecting a series of 1.5-s depolarizing current pulses (−0.1-0.5 nA) in whole-cell current clamp mode. 1-s 470 nm (38.7 mW mm^{-2}) light stimulation was applied in the middle of current injections with 30-s inter-trial-interval. Resting membrane potentials, input resistances, and capacitances were measured in the trials with −0.1 nA current injection. To examine the excitatory effect of the ACRs, 10-ms 470 nm (38.7 mW mm^{-2}) light stimulation was applied, and ACR^- neurons were clamped at −70 mV to record excitatory post-synaptic currents.

After electrophysiology recordings, fluorescent images of the brain slices were acquired on an Axio Zoom.V16 Fluorescence Stereo Zoom Microscope (Zeiss) and processed using MATLAB2024b (MathWorks). Images were taken from 20 brain slices of two male and two female mice.

Generation of transgenic C. elegans strains and EPG recording

The transgenic *C. elegans* strains COP2831 and COP2832 [*uncp*-17::*Ans*ACR::EYFP::*tbb-2u*], *unc-119*(+))} II; *unc-119(ed3)* III expressing *Ans*ACR in cholinergic neurons were created by InVivo Biosystems using the Mos1-mediated Single Copy Insertion (MosSCI) method, which enables integrating the transgene as a single-copy insertion at a designated locus in the *C. elegans* genome (Frokjaer-Jensen 2015). *Unc*-119 rescue cassette insertion was used to bring the transgene into a Mos1 target locus on chromosome II and create rescue of the function of the *unc-119(ed3)* III mutant allele. The Mos1 locus was selected for position-neutral effects and to avoid the gene coding regions, introns, and transcription factor binding sites. The integration of the transgene was confirmed by PCR.

The transgenic and Bristol N2 wild-type worms were grown at 20°C on *E. coli* strain OP50 lawns in the absence or presence of 10 µM (final concentration) all-*trans*-retinal (Millipore-Sigma, Cat. # 116-31-4), which was mixed with the bacteria before seeding Nematode Growth Medium (NGM) plates. EPG recordings were performed from intact worms sucked into a pipette (Raizen and Avery 1994). The pipettes (200 kΩ resistance) were pulled from borosilicate glass and filled with the External Physiological solution, the composition of which is specified in the above section. The worms were transferred to the same solution supplemented with 10 mM serotonin before the measurements. The data were acquired in the voltage clamp mode of the same Axopatch 200B amplifier used for manual patch clamp recording from HEK293 cells and the same software. The data obtained in two independently created strains were pooled together. The photoexcitation was provided by the Polychrome V light source described above. The frequency of the R1-spikes was calculated using the Event Detection by the Threshold Search function of ClampFit after applying a 2-Hz high-pass digital filter. Further analysis was performed using the Origin Pro 2016 software.

Reproducibility and statistics

Plasmids encoding different ChR variants were randomly assigned to transfect identical cell batches. Three independent transfections were performed on different experimental days; the data obtained were pooled together. In automated patch clamp studies, cells were blindly selected by the machine and randomly drawn into the wells. For an unbiased estimation of the photocurrent amplitude, the data from wells that formed seals with a resistance <500 MΩ were excluded. For a more accurate estimation of the Vr values by plotting the IV curves, wells with a seal resistance <500 MΩ and photocurrents of the absolute magnitude <50 pA at −80 mV were excluded. In manual patch clamp experiments, the cells were selected for patching by inspecting their tag fluorescence; non-fluorescent cells and cells in which no GΩ seal was established or lost during recording were excluded from the analysis. Recordings with the access resistance (Ra) >20 MΩ were excluded from the analysis. In automated and manual patch clamp experiments, the photocurrent traces recorded from different cells transfected with the same construct were considered biological replicates (reported as n values). These values indicate how often the experiments were performed independently. In experiments using continuous light pulses, only one photocurrent trace was recorded from one cell for each condition. To increase the signal-to-noise ratio for computer approximations of the photocurrent traces under single-turnover conditions, six replicates recorded from the same cells were considered technical replicates and averaged for further analysis.

Statistical analysis of the patch clamp data was performed using Origin Pro 2016 software. The normal distribution of the data was not assumed. The non-parametric two-tailed Mann-Whitney and Kolmogorov-Smirnov tests were used to compare the means. No statistical methods were used

to pre-determine sample sizes, but the sample sizes were similar as those reported in the previous publications (Govorunova, Gou et al. 2022, Morizumi, Kim et al. 2023).

In the cortical neuron patch clamp experiments, fluorescently labelled or negative neurons were randomly selected from the densely labelled area of brain slices. The criteria for data exclusion were the same as in manual patch clamp recordings from HEK cells. Statistical analysis of the data was performed using ClampFit 10.7 (Molecular Devices) and Prism 10.3 (GraphPad). The multiple Wilcoxon matched-pairs signed rank test with Benjamini, Krieger, and Yekutieli's corrections was used for evaluating the efficiency of action potential inhibition.

In *C. elegans* experiments, the EPG recordings were excluded from the analysis, if the worm moved out of the illuminated area during recording. No data was excluded in flash photolysis experiments.

Data and materials availability

The numerical data and statistical analyses are provided in the Source Data Files. The sequence information was deposited at the NCBI with GenBank Acc. #PQ657777-PQ657783. The plasmids encoding *Ans*ACR, *Ft*ACR, and *Nl*CCR expression constructs in the pcDNA3.1 vector backbone were deposited at Addgene (plasmids #232598, 232599, and 232600, respectively). The plasmids pAAV-CAG-*Ans*ACR-EYFP and pAAV-CAG-*Ft*ACR-EYFP were deposited at Addgene (plasmids #238347 and #238348, respectively). The recombinant *C. elegans* lines expressing *Ans*ACR in the cholinergic neurons are available from the authors upon request.

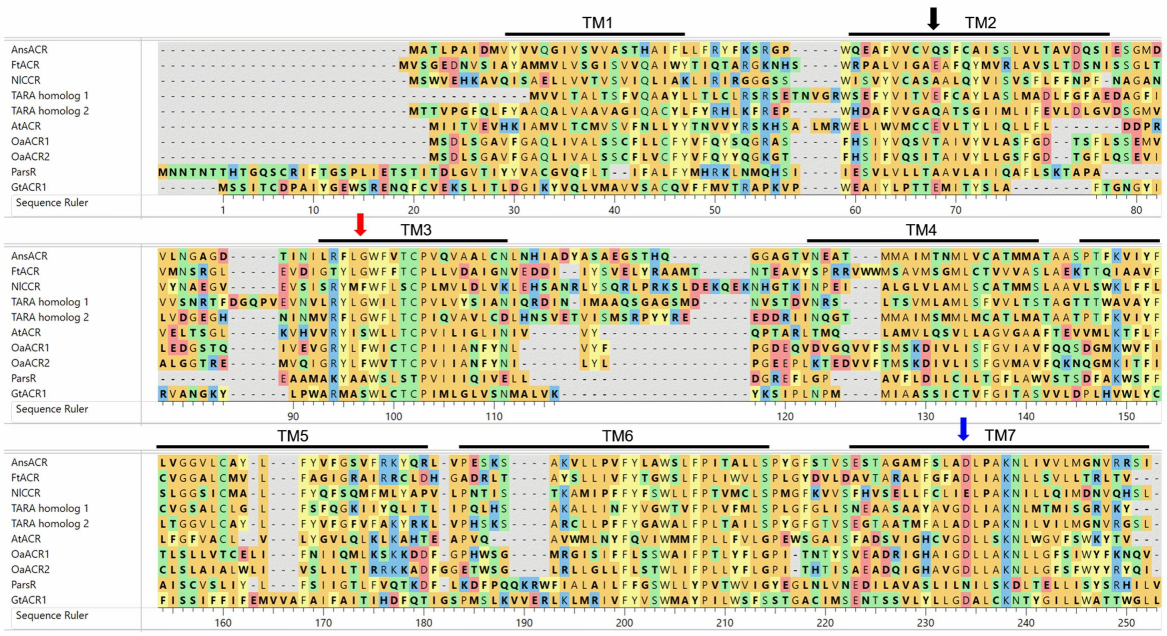

Figure 1 – figure supplement 1.

The protein alignment of the 7TM domains of ChR variants identified and characterized in this study and the previously known *Gt*ACR1.

The amino acid residues are colored according to their chemical properties. The residue ruler is according to the *Gt*ACR1 sequence. The lines show the transmembrane helices TM1-TM7 of *Gt*ACR1. The arrows point to the positions corresponding to Asp68 (black), Ser97 (red), and Asp234 (blue) of *Gt*ACR1.

Figure 1 – figure supplement 2.

Action spectra and photocurrents of ACRs from *Ancoracysta twista* and *Odontella aurita*.

In the left panels, the action spectra. The data points are the mean ± SEM values; n = 6 cells for each variant. In the middle and right panels, the photocurrents recorded by manual patch clamping in the Cl^- bath (middle) and Asp^- bath (right) at the holding voltages increased in 20-mV increments from −60 mV. The dark cyan bars show the duration of illumination (500, 520 and 510 nm, respectively, for *At*ACR, *Oa*ACR1, and *Oa*ACR2).

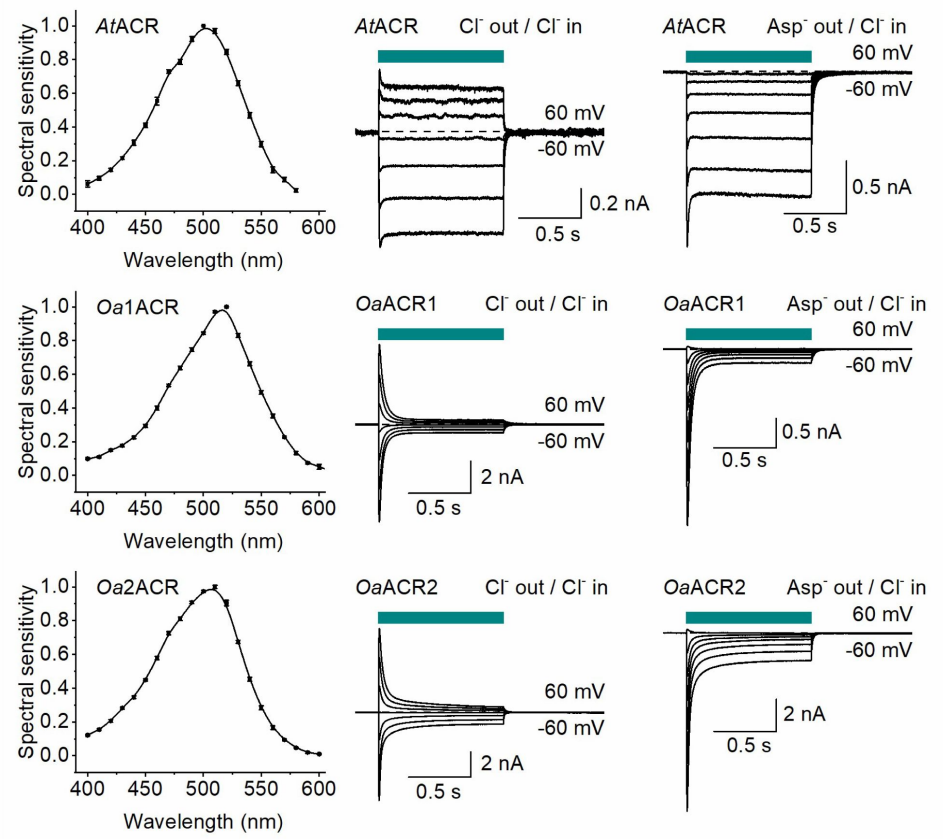

Figure 1 – figure supplement 3.

Comparison of the absorption and action spectra of individual ancyromonad ChRs.

(**A-C**) Overlays of the absorption and action spectra from the main text **Figures 1B and C**.

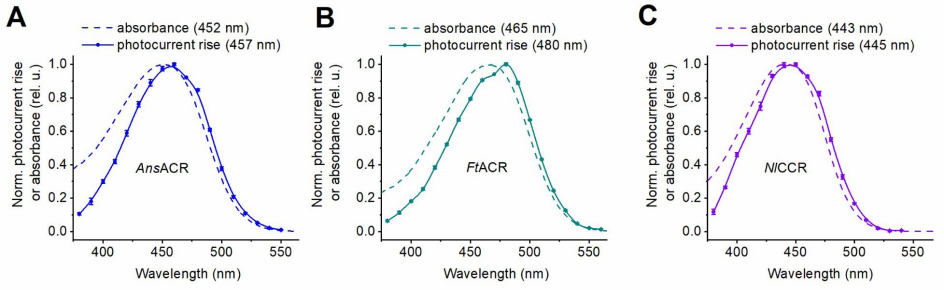

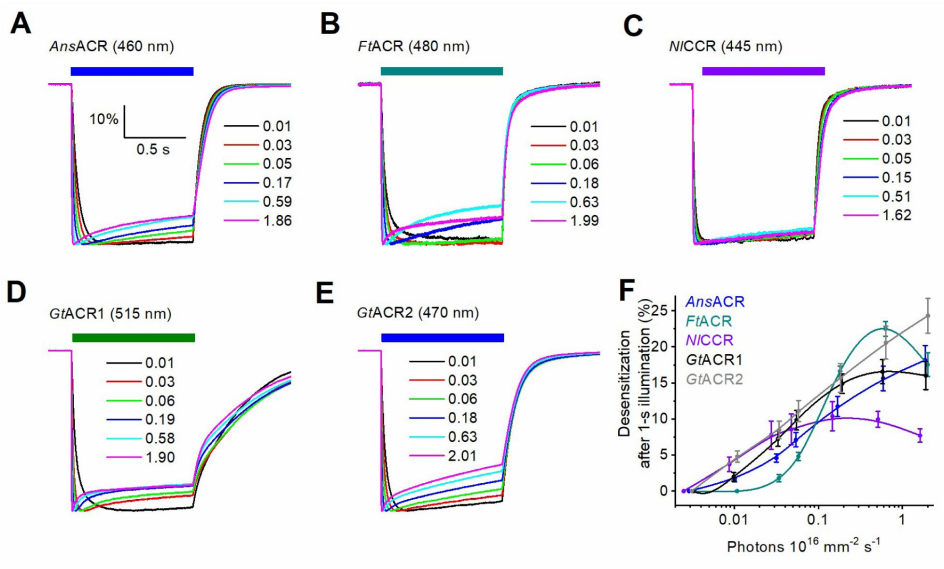

Figure 1 – figure supplement 4.

Desensitization at the end of 1-s illumination.

(**A-E**) Normalized photocurrent traces recorded from the indicated ChRs at −60 mV. The colored rectangles show the duration of illumination. The numbers are photon flux densities multiplied by 10^{16}. (**F**) The dependence of desensitization, calculated as the peak minus end current divided by the peak current and multiplied by 100%, on the photon flux density. The data points are mean ± SEM (n = 8 cells for each variant).

The online version of this article includes the following source data for **Figure 1 – figure supplement 4**:

Source data 1. Source data for the numerical values shown in (F).

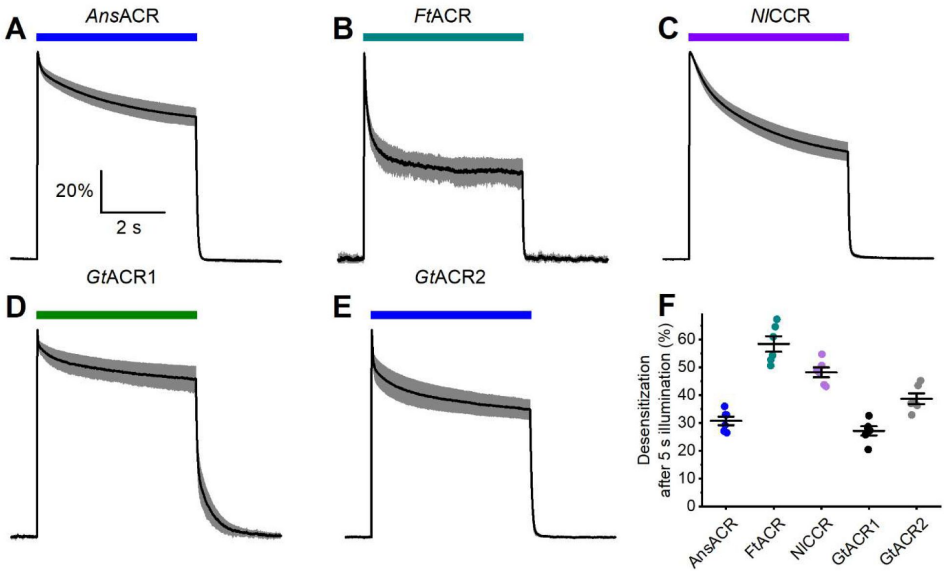

Figure 1 – figure supplement 5.

Desensitization at the end of 5-s illumination.

(**A-E**) Normalized photocurrent traces recorded from the indicated ChRs at +20 mV. The colored rectangles show the duration of illumination. (**F**) Desensitization at the end of illumination. The symbols are data from individual cells, the lines are mean ± SEM, n = 6 cells for each variant.

The online version of this article includes the following source data for **Figure 1 – figure supplement 4**:

Source data 1. Source data for the numerical values shown in (F).

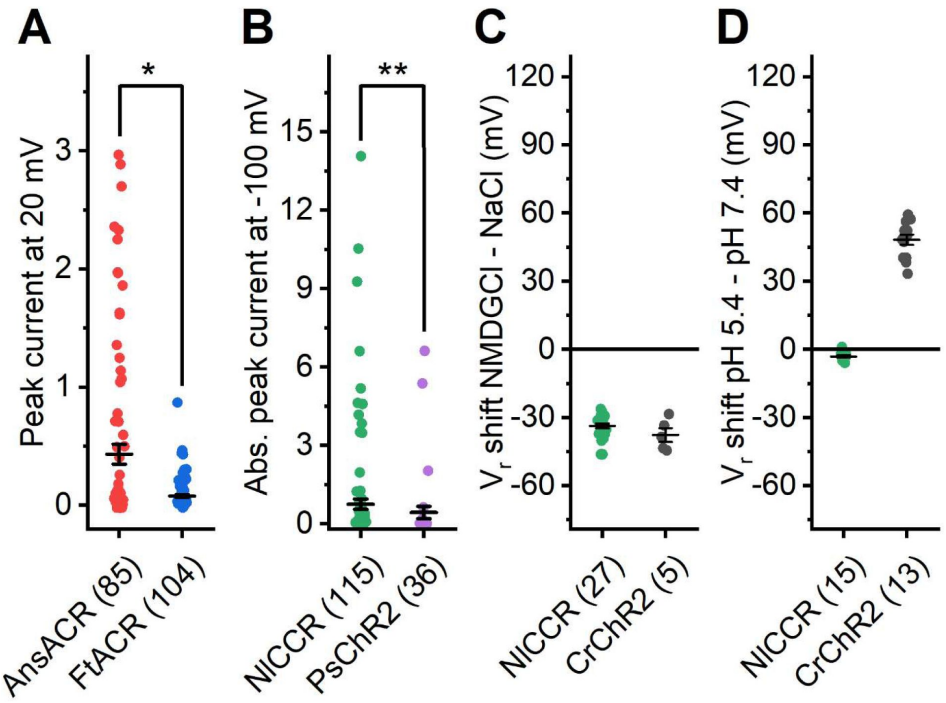

Figure 2 – figure supplement 1.

Photocurrent amplitudes of anycromonad ChRs and comparison of *Nl*CCR with *Cr*ChR2.

(**A, B**) Unbiased estimation of peak photocurrent amplitudes. The photocurrents were recorded at 20 mV for *Ans*ACR and *Ft*ACR, and at −60 mV for *Nl*CCR and *Ps*ChR2. *, p = 0.0047; **, p = 9.9E10-6 by the two-tailed, two-sample Kolmogorov-Smirnov test. (**C, D**) The Vr shifts measured upon replacing Na^+ with $NMDG^+$ in the external solution (C), and upon its acidification from pH 7.4 to 5.4 (D). In all panels, the symbols are the data from individual cells; the lines are the mean and SEM values; the numbers in brackets are the numbers of cells sampled.

The online version of this article includes the following source data for **Figure 2 – figure supplement 1**:

Source data 1. Source data for the numbers of cells sampled and numerical values shown in (A-D).

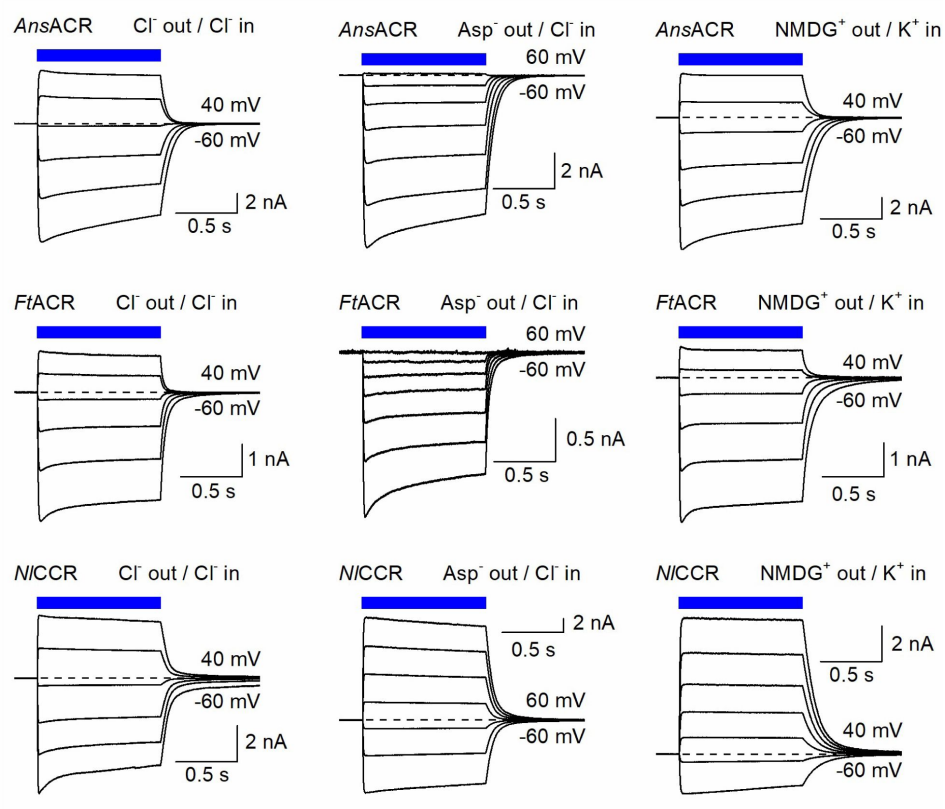

Figure 2 – figure supplement 2.

Photocurrent traces recorded from ancyromonad ChRs by manual patch clamping.

The photocurrents were recorded by manual patch clamping in the Cl^- bath (left), Asp^- bath (middle), and $NMDG^+$ bath (right) at the holding voltages increased in 20-mV increments from −60 mV. The blue bars show the duration of 470 nm illumination.

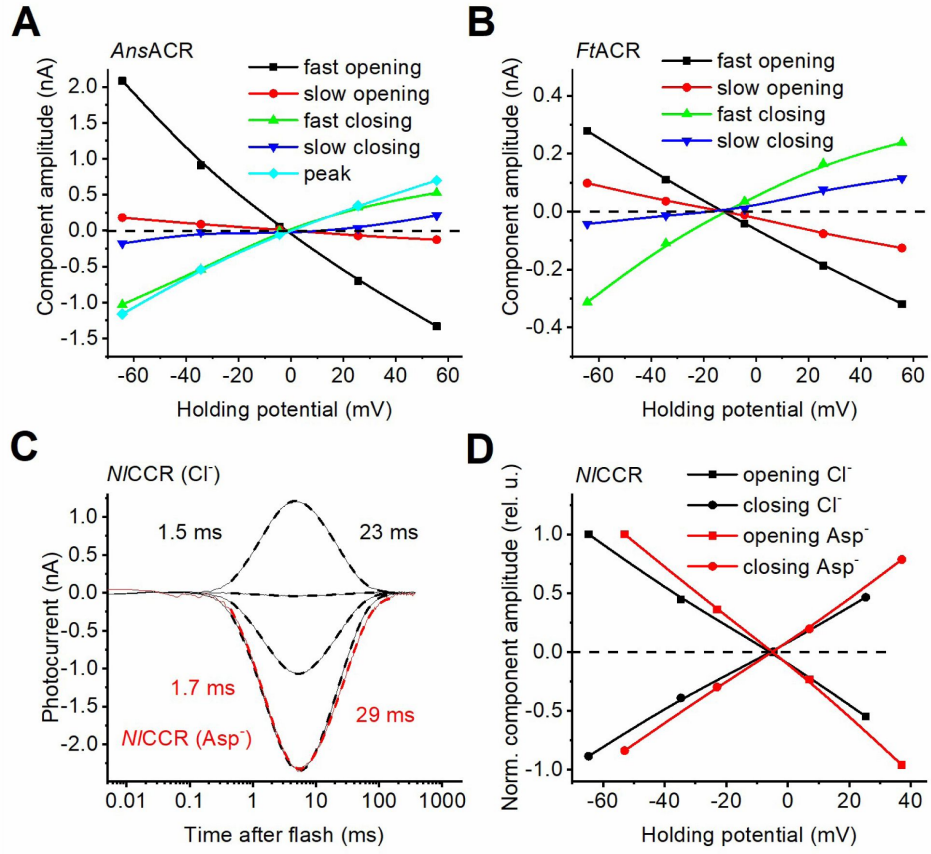

Figure 3 – figure supplement 1.

Current-voltage relationships of photocurrent kinetic components in the three ancyromonad ChRs and laser-flash-evoked *Nl*CCR photocurrents.

(**A, B,** and **D**). The voltage dependence of the amplitudes of the channel closing and opening components estimated by multi-componential approximation of the laser-flash-evoked photocurrents recorded from the indicated ancyromonad ChRs. (**C**) Laser-flash evoked photocurrent traces of *Nl*CCR recorded at the holding voltages increased in 30-mV steps from −60 mV in the Cl^--based bath (black) and at −60 mV in the Asp^--based bath (red). The thin lines are experimental recordings, and the thick dashed lines are multiexponential approximations. The numbers are the τ values of the individual kinetic components.
The online version of this article includes the following source data for **Figure 3 – figure supplement 1**:
Source data 1. Source data for the numerical values shown in (A, B, and D).

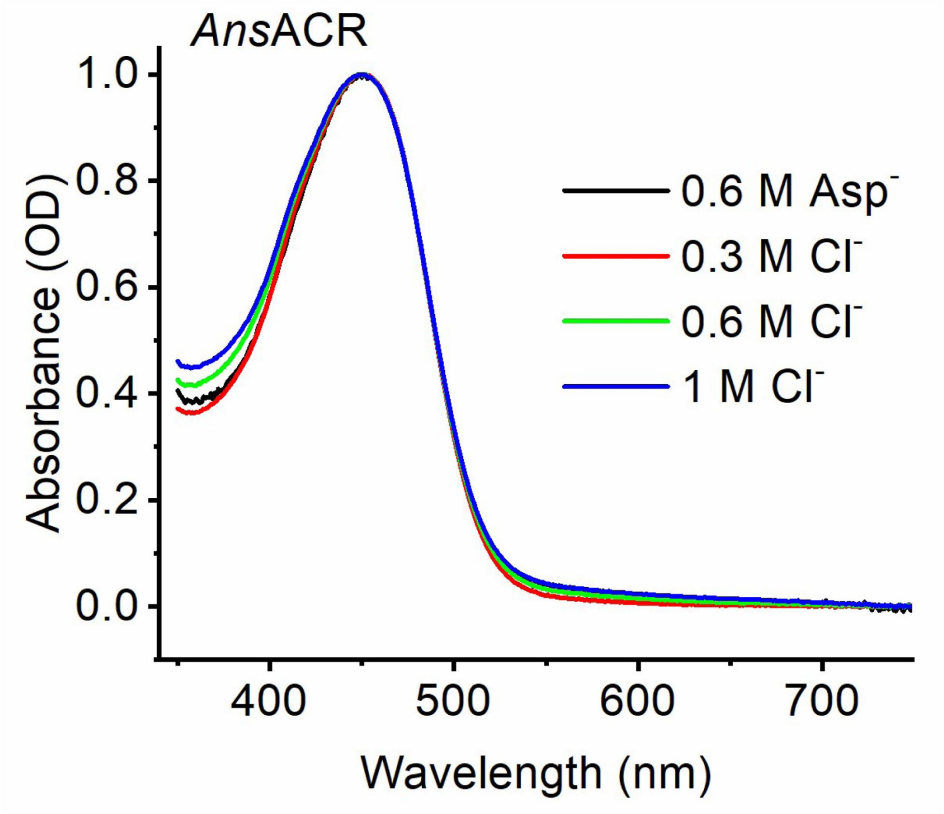

Figure 4 – figure supplement 1.

Dependence of absorption on the Cl^- concentration.

The lines are the absorption spectra of detergent-purified *Ans*ACR at the indicated Cl^- concentrations.

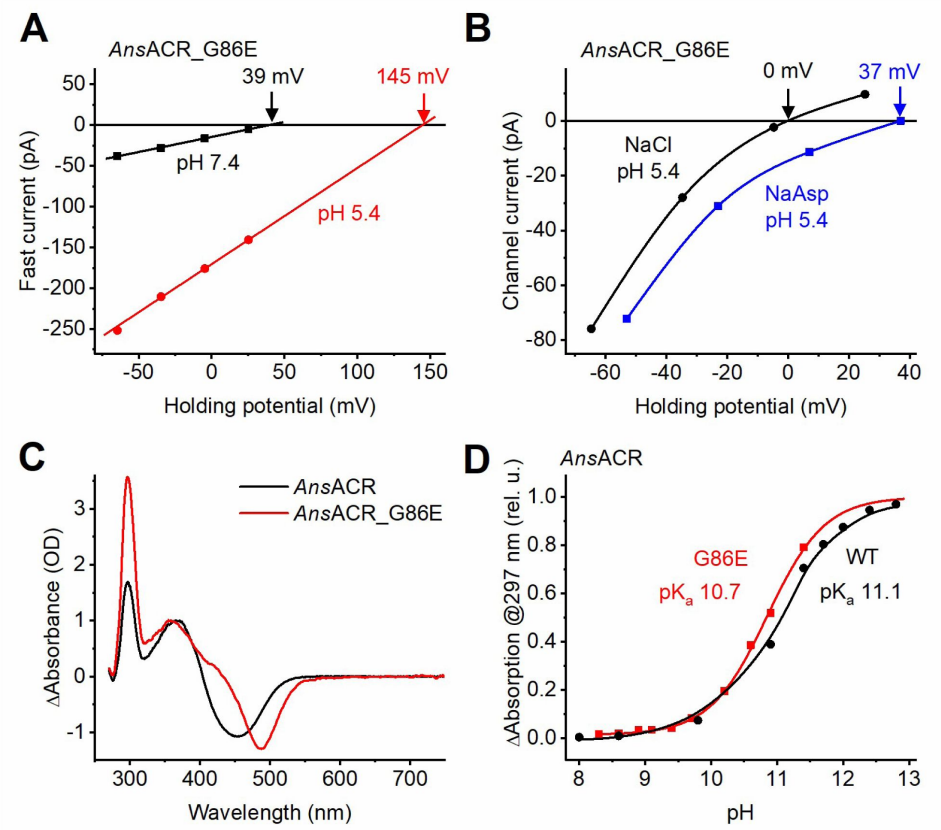

Figure 4 – figure supplement 2.

Continued analysis of the *Ans*ACR_G86E mutant.

(**A**) The voltage dependence of the fast current at pH 7.4 (black) and 5.4 (red). (**B**) The voltage dependence of the channel current at pH 5.4 in the Cl^--based bath (black) and the Asp^--based bath (blue). **(C)** The difference spectra obtained upon alkalization on the purified mutant (red) and WT (black). (**D**) pH titration of the absorbance difference at 297 nm in the purified mutant (red) and WT (black).

The online version of this article includes the following source data for **Figure 4 – figure supplement 2**:

Source data 1. Source data for the numerical values shown in (A, B, and D).

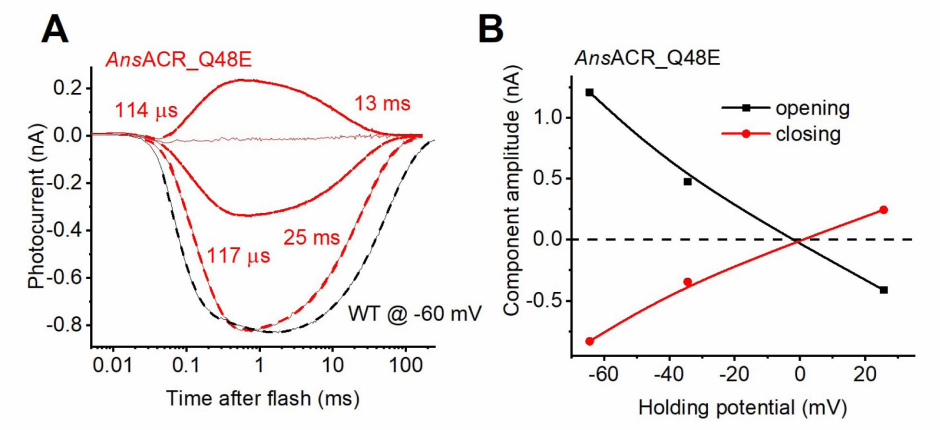

Figure 4 – figure supplement 3.

Photocurrents in the *Ans*ACR_Q48E mutant.

(**A**) Laser-flash evoked photocurrent traces of the mutant recorded at the holding voltages increased in 30-mV steps from −60 mV (red). A trace from the WT at −60 mV (black) is shown for comparison. The thin lines are experimental recordings, and the thick dashed lines are multiexponential approximations. The numbers are the τ values of the individual kinetic components. (**B**) The voltage dependence of the amplitudes of the kinetic components obtained by multiexponential approximation of the laser-flash-evoked photocurrents.

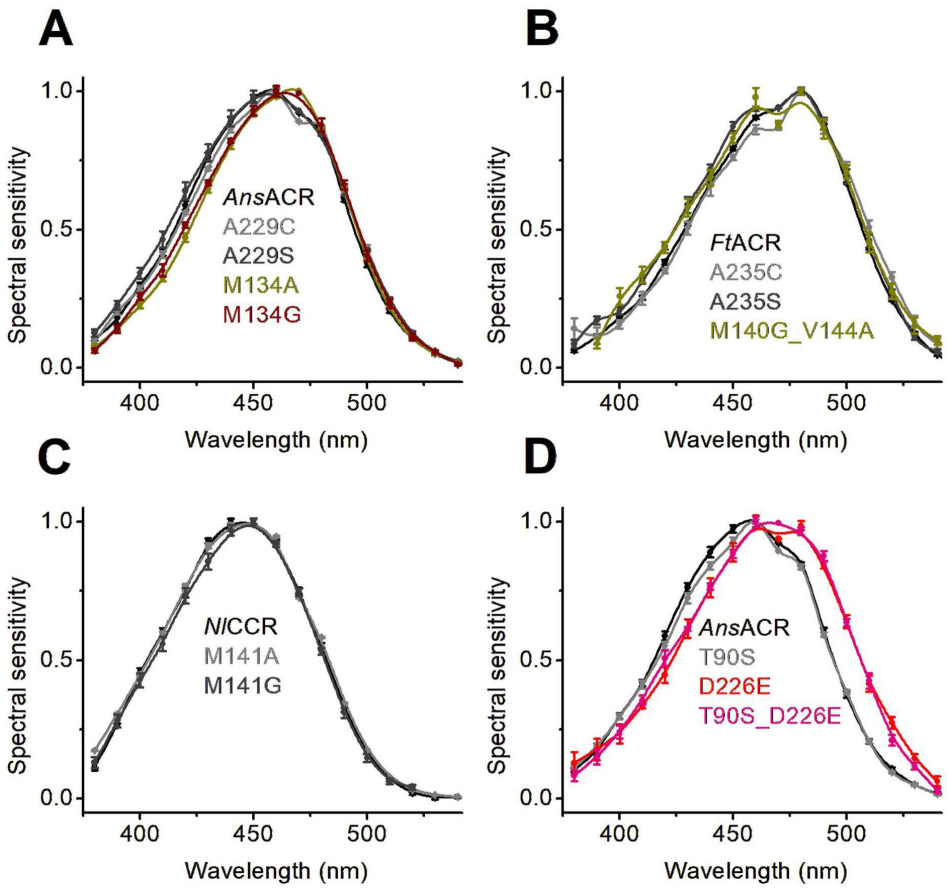

Figure 5 – figure supplement 1.

Mutations blue-shifting other microbial rhodopsins spectra do not affect ancyromonad ChRs.

The photocurrent action spectra of the indicated mutants compared to the respective WTs. The data points are the mean ± SEM values.

The online version of this article includes the following source data for **Figure 5 – figure supplement 1**:

Source data 1. Source data for the numbers of cells sampled and numerical values shown in (A-D).

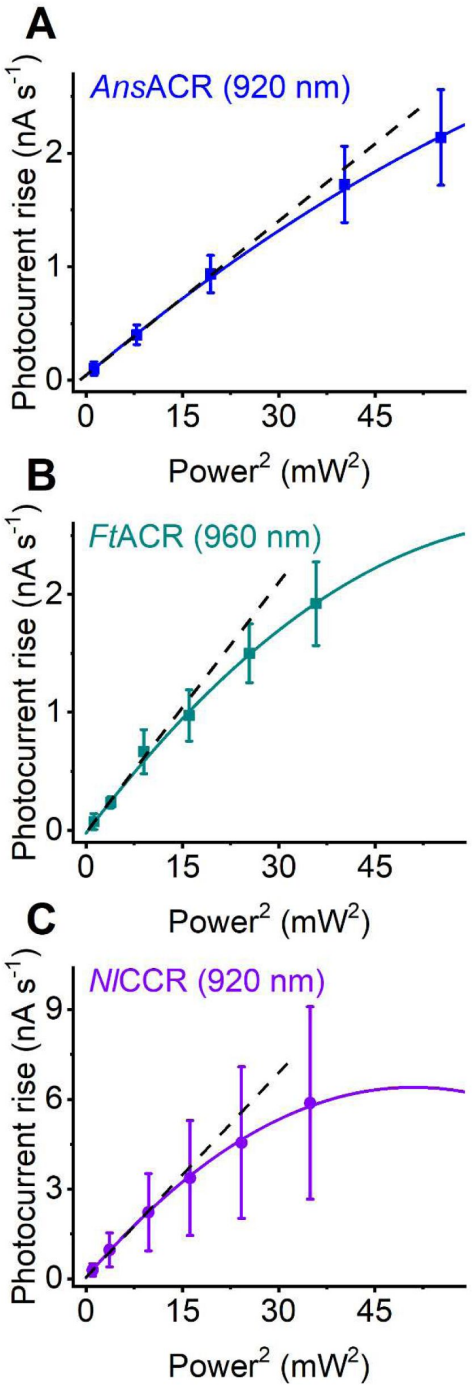

Figure 6 – figure supplement 1.

Power dependence upon 2P illumination.

(**A-C**) The dependence of the photocurrent rise on the quadratic light power. The data points are the mean ± SEM (n = 5 cells for each variant). A 2nd-order polynomial function was fit to the data. The dashed lines show a linear approximation of the initial portion of the curve.

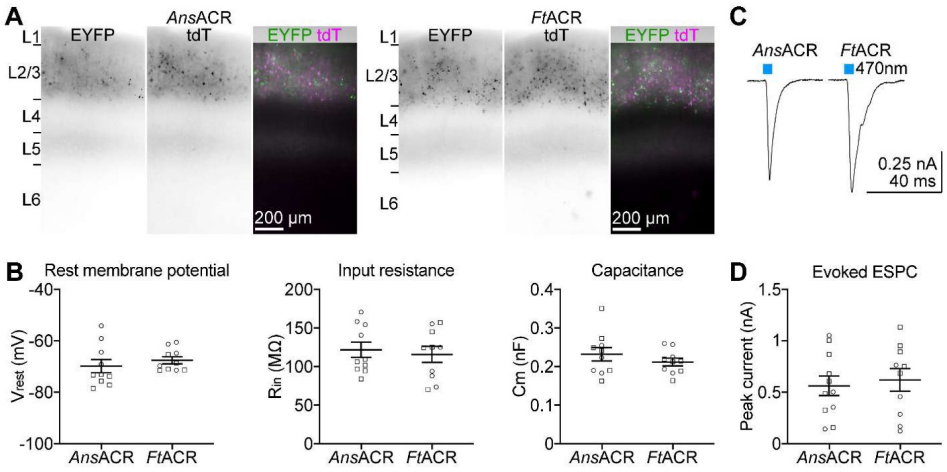

Figure 7 – figure supplement 1.

Characterization of *Ans*ACR and *Ft*ACR expression in cortical neurons and axonal excitatory effect.

(**A**) Representative fluorescence images of 300 µm-thick brain slices expressing tdTomato and EYFP fused to the C termini of *Ans*ACR (left) and *Ft*ACR (right) in cortical layer 2/3 pyramidal neurons. The axons of ACR^{+} layer 2/3 pyramidal neurons ramify in layer 5. L, layer. (**B**) Resting membrane potentials (left), input resistances (middle), and capacitances (right) of *Ans*ACR^{+} and *Ft*ACR^{+} neurons. (**C**) Representative traces of light-evoked excitatory post-synaptic currents (EPSCs) recorded from ACR^{-} pyramidal neurons in layer 2/3 in response to 10-ms 470 nm light pulses (power density of 38.7 mW mm^{-2}). (**D**) Summary data of experiments in (C). The peak currents of light-evoked EPSCs were measured from the averaged current traces of three trials. In all panels, the data points from male mice are indicated by squares and female mice by circles. One male and one female mouse were used for each of the *Ans*ACR and *Ft*ACR experiments. The data points are the mean ± SEM values.
The online version of this article includes the following source data for **Figure 6 – figure supplement 1**:
Source data 1. Source data for the numbers of cells sampled and numerical values shown in (B, D).

Acknowledgements

We thank Dr. Valeria Vasquez (UTHealth) for a generous donation of the wild-type *C. elegans* strain and OP50 *E. coli* strain. We thank Dr. Edward S. Boyden (Massachusetts Institute of Technology) for a gift of the Chrimson plasmid. This work was supported by the National Institutes of Health grants R35GM140838 (J.L.S.), S10OD032293 (J.L.S.), U01NS118288 (M.X., J.L.S., F.S.P.), RF1NS133657 (J.L.S., F.S.P., M.X.), R61CA278458 (F.S.P.), and R01NS136027 (F.S.P.); the Robert A. Welch Foundation Endowed Chair AU-0009 (J.L.S.), and grants Q-2016-20220331 (F.S.P.) and Q-2016-20190330 (F.S.P.); a Vivian L. Smith Endowed Professorship in Neuroscience (F.S.P); the McNair Medical Foundation (F.S.P); the Natural Sciences and Engineering Research Council of Canada (NSERC) grants RGPIN-2018-04397 and RGPIN-2024-03857 (L.S.B.). An NSERC USRA award supported A.P., and S.M. was supported by the President's Research Assistantship (PRA) program at the University of Guelph. M.X. is a Caroline DeLuca Scholar.

Additional information

Supplementary File 1. Compositions and liquid junction potential (LJP) values of the solutions used in automated patch clamp recording.

Supplementary File 2. The wavelength positions of the half-maximal amplitude of the long-wavelength slope of the spectrum (λ50) of ChR variants tested in this study.

Funding

National Institutes of Health (R35GM140838)

National Institutes of Health (S10OD032293)

National Institutes of Health (U01NS118288)

National Institutes of Health (RF1NS133657)

National Institutes of Health (R61CA278458)

National Institutes of Health (R01NS136027)

Welch Foundation (AU-0009)

Welch Foundation (Q-2016-20220331)

Welch Foundation (Q-2016-20190330)

Vivian L. Smith Endowed Professorship in Neuroscience

McNair Medical Foundation

Natural Sciences and Engineering Research Council of Canada (RGPIN-2018-04397)

Natural Sciences and Engineering Research Council of Canada (RGPIN-2024-03857)

NSERC USRA award

University of Guelph (President's Research Assistantship (PRA) program)

Caroline DeLuca Scholar

Additional files

Supplementary File 1

Supplementary File 2

References

Ahrendt S. R., Mondo S. J., Haridas S., Grigoriev I. V. (2023) **MycoCosm, the JGI's fungal genome portal for comparative genomic and multiomics data analyses** *Methods Mol Biol* **2605**:271–291 Google Scholar

Alam I., Kamau A. A., Ngugi D. K., Gojobori T., Duarte C. M., Bajic V. B. (2021) **KAUST Metagenomic Analysis Platform (KMAP), enabling access to massive analytics of re-annotated metagenomic data** *Sci Rep* **11**:11511 Google Scholar

Amses K. R., Simmons D. R., Longcore J. E., Mondo S. J., Seto K., Jeronimo G. H., Bonds A. E., Quandt C. A., Davis W. J., Chang Y., Federici B. A., Kuo A., LaButti K., Pangilinan J., Andreopoulos W., Tritt A., Riley R., Hundley H., Johnson J., Lipzen A., Barry K., Lang B. F., Cuomo C. A., Buchler N. E., Grigoriev I. V., Spatafora J. W., Stajich J. E., James T. Y. (2022) **Diploid-dominant life cycles characterize the early evolution of fungi** *Proc Natl Acad Sci USA* **119**:e2116841119 Google Scholar

Bergs A., Henss T., Glock C., Nagpal J., Gottschalk A. (2022) **Microbial rhodopsin optogenetic tools: Application for analyses of synaptic transmission and of neuronal network activity in behavior** *Methods Mol Biol* **2468**:89–115 Google Scholar

Bhatla N., Droste R., Sando S. R., Huang A., Horvitz H. R. (2015) **Distinct neural circuits control rhythm inhibition and spitting by the myogenic pharynx of C. elegans** *Curr Biol* **25**:2075–2089 Google Scholar

Brown M. W., Heiss A. A., Kamikawa R., Inagaki Y., Yabuki A., Tice A. K., Shiratori T., Ishida K. I., Hashimoto T., Simpson A. G. B., Roger A. J. (2018) **Phylogenomics places orphan protistan lineages in a novel eukaryotic super-group** *Genome Biol Evol* **10**:427–433 Google Scholar

Chen F., Duan X., Yu Y., Yang S., Chen Y., Gee C. E., Nagel G., Zhang K., Gao S., Shen Y. (2022) **Visual function restoration with a highly sensitive and fast Channelrhodopsin in blind mice** *Signal Transduct. Target Ther* **7**:104 Google Scholar

Chen W., Cai Z. L., Chao E. S., Chen H., Longley C. M., Hao S., Chao H. T., Kim J. H., Messier J. E., Zoghbi H. Y., Tang J., Swann J. W., Xue M. (2020) **Stxbp1/Munc18-1 haploinsufficiency impairs inhibition and mediates key neurological features of STXBP1 encephalopathy** *eLife* **9**:e48705 https://doi.org/10.7554/eLife.48705 | Google Scholar

Deisseroth K (2021) **From microbial membrane proteins to the mysteries of emotion** *Cell* **184**:5279–5285 Google Scholar

Doyon N., Vinay L., Prescott S. A., De Koninck Y. (2016) **Chloride regulation: A dynamic equilibrium crucial for synaptic inhibition** *Neuron* **89**:1157–1172 Google Scholar

Emiliani V., Entcheva E., Hedrich R., Hegemann P., Konrad K. R., Lüscher C., Mahn M., Pan Z.-H., Sims R. R., Vierock J., Yizhar O. (2022) **Optogenetics for light control of biological systems** *Nature Reviews Methods Primers* **2**:55 Google Scholar

Engqvist M. K., McIsaac R. S., Dollinger P., Flytzanis N. C., Abrams M., Schor S., Arnold F. H. (2015) **Directed evolution of Gloeobacter violaceus rhodopsin spectral properties** *J. Mol.*

Biol **427**:205–220 Google Scholar

Ernst O. P., Lodowski D. T., Elstner M., Hegemann P., Brown L. S., Kandori H. (2014) **Microbial and animal rhodopsins: structures, functions, and molecular mechanisms** *Chem. Rev* **114**:126–163 Google Scholar

Forli A., Vecchia D., Binini N., Succol F., Bovetti S., Moretti C., Nespoli F., Mahn M., Baker C. A., Bolton M. M., Yizhar O., Fellin T. (2018) **Two-photon bidirectional control and imaging of neuronal excitability with high spatial resolution in vivo** *Cell Rep* **22**:3087–3098 Google Scholar

Frokjaer-Jensen C (2015) **Transposon-Assisted Genetic Engineering with Mos1-Mediated Single-Copy Insertion (MosSCI)** *Methods Mol Biol* **1327**:49–58 Google Scholar

Govorunova E. G., Gou Y., Sineshchekov O. A., Li H., Lu X., Wang Y., Brown L. S., St-Pierre F., Xue M., Spudich J. L. (2022) **Kalium channelrhodopsins are natural light-gated potassium channels that mediate optogenetic inhibition** *Nat. Neurosci* **25**:967–974 Google Scholar

Govorunova E. G., Jung K.-W., Sineshchekov O. A., Spudich J. L. (2004) **Chlamydomonas sensory rhodopsins A and B: Cellular content and role in photophobic responses** *Biophys. J* **86**:2342–2349 Google Scholar

Govorunova E. G., Sineshchekov O. A., Brown L. S., Spudich J. L. (2022) **Biophysical characterization of light-gated ion channels using planar automated patch clamp** *Front. Mol. Neurosci* **15**:976910 Google Scholar

Govorunova E. G., Sineshchekov O. A., Li H., Janz R., Spudich J. L. (2013) **Characterization of a highly efficient blue-shifted channelrhodopsin from the marine alga Platymonas subcordiformis** *J. Biol. Chem* **288**:29911–29922 Google Scholar

Govorunova E. G., Sineshchekov O. A., Li H., Wang Y., Brown L. S., Palmateer A., Melkonian M., Cheng S., Carpenter E., Patterson J., Wong G. K. S., Spudich J. L. (2021) **Cation and anion channelrhodopsins: Sequence motifs and taxonomic distribution** *MBio* **12**:e0165621 Google Scholar

Govorunova E. G., Sineshchekov O. A., Li H., Wang Y., Brown L. S., Spudich J. L. (2020) **RubyACRs, non-algal anion channelrhodopsins with highly red-shifted absorption** *Proc. Natl. Acad. Sci. USA* **117**:22833–22840 Google Scholar

Govorunova E. G., Sineshchekov O. A., Liu X., Janz R., Spudich J. L. (2015) **Natural light-gated anion channels: A family of microbial rhodopsins for advanced optogenetics** *Science* **349**:647–650 Google Scholar

Govorunova E. G., Sineshchekov O. A., Spudich J. L. (2022) **Emerging diversity of channelrhodopsins and their structure-function relationships** *Front Cell Neurosci* **15**:800313 Google Scholar

Govorunova E. G., Sineshchekov O. A., Spudich J. L. (2023) **Potassium-selective channelrhodopsins** *Biophysics and Physicobiology* **20**:e201011 Google Scholar

Hoang D. T., Chernomor O., von Haeseler A., Minh B. Q., Vinh L. S. (2018) **UFBoot2: Improving the ultrafast bootstrap approximation** *Mol. Biol. Evol* **35**:518–522 Google Scholar

Hochbaum D.R., Zhao Y., Farhi S.L., Klapoetke N., Werley C.A., Kapoor V., Zou P., Kralj J.M., Maclaurin D., Smedemark-Margulies N., Saulnier J.L., Boulting, G.L., Straub C., Cho Y.K., Melkonian M., Wong G.K., Harrison, D.J., Murthy V.N., Sabatini B.L., Boyden E.S., Campbell R.E., Cohen A.E (2014) **All-optical electrophysiology in mammalian neurons using engineered microbial rhodopsins** *Nat. Methods* **8**:825–833 Google Scholar

Hoffmann M., Wanko M., Strodel P., Konig P.H., Frauenheim T., Schulten K., Thiel W., Tajkhorshid E., Elstner M (2006) **Color tuning in rhodopsins: the mechanism for the spectral shift between bacteriorhodopsin and sensory rhodopsin II** *J. Am. Chem. Soc* **128**:10808–10818 Google Scholar

Inoue K., Del Carmen Marin M., Tomida S., Nakamura R., Nakajima Y., Olivucci M., Kandori H. (2019) **Red-shifting mutation of light-driven sodium-pump rhodopsin** *Nat. Commun* **10**:1993 Google Scholar

Janouškovec J., Tikhonenkov D. V., Burki F., Howe A. T., Rohwer F. L., Mylnikov A. P., Keeling P. J. (2017) **A new lineage of eukaryotes illuminates early mitochondrial genome reduction** *Curr Biol* **27**:3717–3724 Google Scholar

Karasuyama M., Inoue K., Nakamura R., Kandori H., Takeuchi I. (2018) **Understanding colour tuning rules and predicting absorption wavelengths of microbial rhodopsins by data-driven machine-learning approach** *Sci. Rep* **8**:15580 Google Scholar

Kato H. E., Kamiya M., Sugo S., Ito J., Taniguchi R., Orito A., Hirata K., Inutsuka A., Yamanaka A., Maturana A. D., Ishitani R., Sudo Y., Hayashi S., Nureki O. (2015) **Atomistic design of microbial opsin-based blue-shifted optogenetics tools** *Nat. Commun* **6**:7177 Google Scholar

Kim Y. S., Kato H. E., Yamashita K., Ito S., Inoue K., Ramakrishnan C., Fenno L. E., Evans K. E., Paggi J. M., Dror R. O., Kandori H., Kobilka B. K., Deisseroth K. (2018) **Crystal structure of the natural anion-conducting channelrhodopsin GtACR1** *Nature* **561**:343–348 Google Scholar

Letunic I., Bork P. (2024) **Interactive Tree of Life (iTOL) v6: recent updates to the phylogenetic tree display and annotation tool** *Nucleic Acids Res* **52**:W78–W82 Google Scholar

Li H., Huang C. Y., Govorunova E. G., Schafer C. T., Sineshchekov O. A., Wang M., Zheng L., Spudich J. L. (2019) **Crystal structure of a natural light-gated anion channelrhodopsin** *eLife* **8**:e41741 Google Scholar

Mahn M., Gibor L., Patil P., Cohen-Kashi Malina K., Oring S., Printz Y., Levy R., Lampl I., Yizhar O. (2018) **High-efficiency optogenetic silencing with soma-targeted anion-conducting channelrhodopsins** *Nat. Commun* **9**:4125 Google Scholar

Man D., Wang W., Sabehi G., Aravind L., Post A. F., Massana R., Spudich E. N., Spudich J. L., Béjà O. (2003) **Diversification and spectral tuning in marine proteorhodopsins** *EMBO J* **22**:1725–1731 Google Scholar

Mardinly A. R., Oldenburg I. A., Pegard N. C., Sridharan S., Lyall E. H., Chesnov K., Brohawn S. G., Waller L., Adesnik H. (2018) **Precise multimodal optical control of neural ensemble activity** *Nat. Neurosci* **21**:881–893 Google Scholar

Messier J. E., Chen H., Cai Z. L., Xue M. (2018) **Targeting light-gated chloride channels to neuronal somatodendritic domain reduces their excitatory effect in the axon** *eLife* **7**:e38506 Google Scholar

Minh B. Q., Schmidt H. A., Chernomor O., Schrempf D., Woodhams M. D., von Haeseler A., Lanfear R. (2020) **IQ-TREE 2: New models and efficient methods for phylogenetic inference in the genomic era** *Mol. Biol. Evol* **37**:1530–1534 Google Scholar

Morizumi T., Kim K., Li H., Govorunova E. G., Sineshchekov O. A., Wang Y., Zheng L., Bertalan E., Bondar A. N., Askari A., Brown L. S., Spudich J. L., Ernst O. P. (2023) **Structures of channelrhodopsin paralogs in peptidiscs explain their contrasting K+ and Na+ selectivities** *Nat Commun* **14**:4365 Google Scholar

Nanjappa D., Sanges R., Ferrante M. I., Zingone A. (2017) **Diatom flagellar genes and their expression during sexual reproduction in Leptocylindrus danicus** *BMC Genomics* **18**:813 Google Scholar

Oda K., Vierock J., Oishi S., Rodriguez-Rozada S., Taniguchi R., Yamashita K., Wiegert J. S., Nishizawa T., Hegemann P., Nureki O. (2018) **Crystal structure of the red light-activated channelrhodopsin Chrimson** *Nat. Commun* **9**:3949 Google Scholar

Oppermann J., Rozenberg A., Fabrin T., Gonzalez-Cabrera C., Parker R., Beja O., Prigge M., Hegemann P. (2024) **Robust optogenetic inhibition with red-light-sensitive anion-conducting channelrhodopsins** *eLife* **12**:RP90100 Google Scholar

Pereira L., Kratsios P., Serrano-Saiz E., Sheftel H., Mayo A. E., Hall D. H., White J. G., LeBoeuf B., Garcia L. R., Alon U., Hobert O. (2015) **A cellular and regulatory map of the cholinergic nervous system of C. elegans** *eLife* **4**:e12432 https://doi.org/10.7554/eLife.12432 | Google Scholar

Piatkevich K. D., Boyden E. S. (2023) **Optogenetic control of neural activity: the Biophysics of microbial rhodopsins in neuroscience** *Q Rev Biophys* **57**:1–26 Google Scholar

Priyam A., Woodcroft B. J., Rai V., Moghul I., Munagala A., Ter F., Chowdhary H., Pieniak I., Gibbins M. A., Moon H., Davis-Richardson A., Uludag M., Watson-Haigh N. S., Challis R., Nakamura H., Favreau E., Gomez E. A., Pluskal T., Leonard G., Rumpf W., Wurm Y. (2019) **Sequenceserver: A modern graphical user interface for custom BLAST databases** *Mol Biol Evol* **36**:2922–2924 Google Scholar

Raizen D. M., Avery L. (1994) **Electrical activity and behavior in the pharynx of Caenorhabditis elegans** *Neuron* **12**:483–495 Google Scholar

Richter D. J., Berney C., Strassert J. F. H., Poh Y.-P., Herman E. K., Muñoz-Gómez S. A., Wideman J. G., Burki F., de Vargas C. (2022) **EukProt: A database of genome-scale predicted proteins across the diversity of eukaryotes** *Peer Community Journal* **2**:e56 Google Scholar

Rozenberg A. (2024) **A catalog of natural channelrhodopsins** *Zenodo* 1.5

Rozenberg A., Oppermann J., Wietek J., Fernandez Lahore R. G., Sandaa R. A., Bratbak G., Hegemann P., Béjà O. (2020) **Lateral gene transfer of anion-conducting channelrhodopsins between green algae and giant viruses** *Curr. Biol* **30**:4910–4920 Google Scholar

Sakamoto M., Yokoyama T. (2025) **Probing neuronal activity with genetically encoded calcium and voltage fluorescent indicators** *Neurosci Res* **215**:56–63 Google Scholar

Schuler C., Fischer E., Shaltiel L., Steuer Costa W., Gottschalk A. (2015) **Arrhythmogenic effects of mutated L-type Ca2+-channels on an optogenetically paced muscular pump in Caenorhabditis elegans** *Sci Rep* **5**:14427 Google Scholar

Shimono K., Iwamoto M., Sumi M., Kamo N. (2000) **Effects of three characteristic amino acid residues of pharaonis phoborhodopsin on the absorption maximum** *Photochem. Photobiol* **72**:141–145 Google Scholar

Shimono K., Kitami M., Iwamoto M., Kamo N. (2000) **Involvement of two groups in reversal of the bathochromic shift of pharaonis phoborhodopsin by chloride at low pH** *Biophys. Chem* **87**:225–230 Google Scholar

Sineshchekov O. A., Govorunova E. G., Li H., Spudich J. L. (2015) **Gating mechanisms of a natural anion channelrhodopsin** *Proc. Natl. Acad. Sci. USA* **112**:14236–14241 Google Scholar

Sineshchekov O. A., Govorunova E. G., Li H., Wang Y., Spudich J. L. (2023) **Sequential absorption of two photons creates a bistable form of RubyACR responsible for its strong desensitization** *Proc Natl Acad Sci U S A* **120**:e2301521120 Google Scholar

Sineshchekov O. A., Jung K.-H., Spudich J. L. (2002) **Two rhodopsins mediate phototaxis to low- and high-intensity light in Chlamydomonas reinhardtii** *Proc. Natl. Acad. Sci. USA* **99**:8689–8694 Google Scholar

Sineshchekov O. A., Li H., Govorunova E. G., Spudich J. L. (2016) **Photochemical reaction cycle transitions during anion channelrhodopsin gating** *Proc. Natl. Acad. Sci. USA* **113**:E1993–2000 Google Scholar

Spudich E. N., Ozorowski G., Schow E. V., Tobias D. J., Spudich J. L., Luecke H. (2012) **A transporter converted into a sensor, a phototaxis signaling mutant of bacteriorhodopsin at 3.0 A** *J. Mol. Biol* **415**:455–463 Google Scholar

Spudich J. L (2022) **LogPro** *Zenodo* Google Scholar

Sudo Y., Okazaki A., Ono H., Yagasaki J., Sugo S., Kamiya M., Reissig L., Inoue K., Ihara K., Kandori H., Takagi S., Hayashi S. (2013) **A blue-shifted light-driven proton pump for neural silencing** *J. Biol. Chem* **288**:20624–20632 Google Scholar

Sunagawa S., Coelho L. P., Chaffron S., Kultima J. R., Labadie K., Salazar G., Djahanschiri B., Zeller G., Mende D. R., Alberti A., Cornejo-Castillo F. M., Costea P. I., Cruaud C., d'Ovidio F., Engelen S., Ferrera I., Gasol J. M., Guidi L., Hildebrand F., Kokoszka F., Lepoivre C., Lima-Mendez G., Poulain J., Poulos B. T., Royo-Llonch M., Sarmento H., Vieira-Silva S., Dimier C., Picheral M., Searson S., Kandels-Lewis S., Tara Oceans Collaborators, Bowler C., de Vargas C., Gorsky G., Grimsley N., Hingamp, Iudicone D., Jaillon O., Not F., Ogata H., Pesant S., Speich S., Stemmann L., Sullivan M.B., Weissenbach J., Wincker P., Karsenti E., Raes J., Acinas S.G., Bork P (2015) **Structure and function of the global ocean microbiome** *Science* **348**:1261359 Google Scholar

Tajima S., Kim Y. S., Fukuda M., Jo Y., Wang P. Y., Paggi J. M., Inoue M., Byrne E. F. X., Kishi K. E., Nakamura S., Ramakrishnan C., Takaramoto S., Nagata T., Konno M., Sugiura M., Katayama K., Matsui T. E., Yamashita K., Kim S., Ikeda H., Kim J., Kandori H., Dror R. O., Inoue K., Deisseroth K., Kato H. E. (2023) **Structural basis for ion selectivity in potassium-selective channelrhodopsins** *Cell* **186**:4325–4344 Google Scholar

Tashiro R., Sushmita K., Hososhima S., Sharma S., Kateriya S., Kandori H., Tsunoda S. P. (2021) **Specific residues in the cytoplasmic domain modulate photocurrent kinetics of channelrhodopsin from the alga Klebsormidium nitens." Commun** *Biol* **4**:235 Google Scholar

Tikhonenkov D. V., Mikhailov K. V., Gawryluk R. M. R., Belyaev A. O., Mathur V., Karpov S. A., Zagumyonnyi D. G., Borodina A. S., Prokina K. I., Mylnikov A. P., Aleoshin V. V., Keeling P. J. (2022) **Microbial predators form a new supergroup of eukaryotes** *Nature* **612**:714–719 Google Scholar

Torruella G., de Mendoza A., Grau-Bove X., Anto M., Chaplin M. A., del Campo J., Eme L., Perez-Cordon G., Whipps C. M., Nichols K. M., Paley R., Roger A. J., Sitja-Bobadilla A., Donachie S., Ruiz-Trillo I. (2015) **Phylogenomics reveals convergent evolution of lifestyles in close relatives of animals and fungi** *Curr Biol* **25**:2404–2410 Google Scholar

Trojanowski N. F., Padovan-Merhar O., Raizen D. M., Fang-Yen C. (2014) **Neural and genetic degeneracy underlies Caenorhabditis elegans feeding behavior** *J Neurophysiol* **112**:951–961 Google Scholar

Trojanowski N. F., Raizen D. M., Fang-Yen C. (2016) **Pharyngeal pumping in Caenorhabditis elegans depends on tonic and phasic signaling from the nervous system** *Sci Rep* **6**:22940 Google Scholar

Tsujimura M., Noji T., Saito K., Kojima K., Sudo Y., Ishikita H. (2021) **Mechanism of absorption wavelength shifts in anion channelrhodopsin-1 mutants** *Biochim. Biophys. Acta Bioenerg* **1862**:148349 Google Scholar

Tucker K., Sridharan S., Adesnik H., Brohawn S. G. (2022) **Cryo-EM structures of the channelrhodopsin ChRmine in lipid nanodiscs** *Nat Commun* **13**:4842 Google Scholar

Váró G., Brown L. S., Needleman R., Lanyi J. K. (1996) **Proton transport by halorhodopsin** *Biochemistry* **35**:6604–6611 Google Scholar

Villar E., Vannier T., Vernette C., Lescot M., Cuenca M., Alexandre A., Bachelerie P., Rosnet T., Pelletier E., Sunagawa S., Hingamp P. (2018) **The Ocean Gene Atlas: exploring the biogeography of plankton genes online** *Nucleic Acids Res* **46**:W289–W295 Google Scholar

(2017) **Volkov, O., K. Kovalev, V. Polovinkin, V. Borshchevskiy, C. Bamann, R. Astashkin, E. Marin, A. Popov, T. Balandin, D. Willbold, G. Buldt, E. Bamberg and V. Gordeliy (2017). "Structural insights into ion conduction by channelrhodopsin 2." Science 358(6366): eaan8862.** Google Scholar

Wang Y. Z., Natsume K., Tanaka T., Hososhima S., Tashiro R., Sano F. K., Akasaka H., Tsunoda S. P., Shihoya W., Kandori H., Nureki O. (2025) **Cryo-EM structure of a blue-shifted channelrhodopsin from Klebsormidium nitens** *Nat Commun* **16**:5297 Google Scholar

Xue M., Atallah B. V., Scanziani M. (2014) **Equalizing excitation-inhibition ratios across visual cortical neurons** *Nature* **511**:596–600 Google Scholar

Zabelskii D., Alekseev A., Kovalev K., Rankovic V., Balandin T., Soloviov D., Bratanov D., Savelyeva E., Podolyak E., Volkov D., Vaganova S., Astashkin R., Chizhov I., Yutin N., Rulev M., Popov A., Eria-Oliveira A. S., Rokitskaya T., Mager T., Antonenko Y., Rosselli R., Armeev G., Shaitan K., Vivaudou M., Buldt G., Rogachev A., Rodriguez-Valera F., Kirpichnikov M., Moser T.,

Offenhausser A., Willbold D., Koonin E., Bamberg E., Gordeliy V. (2020) **Viral rhodopsins 1 are an unique family of light-gated cation channels** *Nat. Commun* **11**:5707 Google Scholar

Author information

Elena G Govorunova
Center for Membrane Biology, Department of Biochemistry & Molecular Biology, The University of Texas Health Science Center at Houston McGovern Medical School, Houston, United States
ORCID iD: 0000-0003-0522-9683

Oleg A Sineshchekov
Center for Membrane Biology, Department of Biochemistry & Molecular Biology, The University of Texas Health Science Center at Houston McGovern Medical School, Houston, United States

Hai Li
Center for Membrane Biology, Department of Biochemistry & Molecular Biology, The University of Texas Health Science Center at Houston McGovern Medical School, Houston, United States
ORCID iD: 0000-0002-3969-6709

Yueyang Gou
Department of Neuroscience, Baylor College of Medicine, Houston, United States, The Cain Foundation Laboratories, Jan and Dan Duncan Neurological Research Institute at Texas Children's Hospital, Houston, United States

Hongmei Chen
Department of Neuroscience, Baylor College of Medicine, Houston, United States, The Cain Foundation Laboratories, Jan and Dan Duncan Neurological Research Institute at Texas Children's Hospital, Houston, United States

Shuyuan Yang
Department of Chemical and Biomolecular Engineering, Rice University, Houston, United States

Yumei Wang
Center for Membrane Biology, Department of Biochemistry & Molecular Biology, The University of Texas Health Science Center at Houston McGovern Medical School, Houston, United States

Stephen Mitchell
Department of Physics and Biophysics Interdepartmental Group, University of Guelph, Guelph, Canada

Alyssa Palmateer
Department of Physics and Biophysics Interdepartmental Group, University of Guelph, Guelph, Canada

Leonid S Brown
Department of Physics and Biophysics Interdepartmental Group, University of Guelph, Guelph, Canada

François St-Pierre
Department of Neuroscience, Baylor College of Medicine, Houston, United States, Department of Biochemistry and Molecular Biology, Baylor College of Medicine, Houston, United States, Systems, Synthetic, and Physical Biology Program, Rice University, Houston, United States, Department of Electrical and Computer Engineering, Rice University, Houston, United States
ORCID iD: 0000-0001-8618-4135

Mingshan Xue
Department of Neuroscience, Baylor College of Medicine, Houston, United States, The Cain Foundation Laboratories, Jan and Dan Duncan Neurological Research Institute at Texas Children's Hospital, Houston, United States, Department of Molecular and Human Genetics, Baylor College of Medicine, Houston, United States
ORCID iD: 0000-0003-1463-8884

John L Spudich
Center for Membrane Biology, Department of Biochemistry & Molecular Biology, The University of Texas Health Science Center at Houston McGovern Medical School, Houston, United States
ORCID iD: 0000-0003-4167-8590

For correspondence: john.l.spudich@uth.tmc.edu

Editors

Reviewer #1 (Public review):

Summary:

This work by Govorunova et al. identified three naturally blue-shifted channelrhodopsins (ChRs) from ancyromonads, namely AnsACR, FtACR, and NlCCR. The phylogenetic analysis places the ancyromonad ChRs in a distinct branch, highlighting their unique evolutionary origin and potential for novel applications in optogenetics. Further characterization revealed the spectral sensitivity, ionic selectivity, and kinetics of the newly discovered AnsACR, FtACR, and NlCCR. This study also offers valuable insights into the molecular mechanism underlying the function of these ChRs, including the roles of specific residues in the retinal-binding pocket. Finally, this study validated the functionality of these ChRs in both mouse brain slices (for AnsACR and FtACR) and in vivo in Caenorhabditis elegans (for AnsACR), demonstrating the versatility of these tools across different experimental systems.
In summary, this work provides a potentially valuable addition to the optogenetic toolkit by identifying and characterizing novel blue-shifted ChRs with unique properties.

Strengths:

This study provides a thorough characterization of the biophysical properties of the ChRs' properties and demonstrated the versatility of these tools in different ex vivo and in vivo experimental systems. The authors also explored the potential of AnsACR for multiplexed optogenetics. Finally, the mutagenesis experiments revealed the roles of key residues in the photoactive site that can affect the spectral and kinetic properties of the channelrhodopsins.

Weaknesses:

The revised manuscript has addressed most of the previous major weaknesses.

https://doi.org/10.7554/eLife.106508.2.sa3

Reviewer #2 (Public review):

Summary:

Govorunova et al present three new anion opsins that have potential applications silencing neurons. They identify new opsins by scanning numerous databases for sequence homology to known opsins, focusing on anion opsins. The three opsin identified, are uncommonly fast, potent, and are able to silence neuronal activity. The authors characterize numerous parameters of the opsins and compare these opsins to the existing and widely used GtACR opsins.

Strengths:

This paper follows the tradition of the Spudich lab, presenting and rigorously characterizing potentially valuable opsins. Furthermore, they explore several mutations of the identified opsin that may make these opsins even more useful for the broader community. The opsins AnsACR and FtACR are particularly notable having extraordinarily fast onset kinetics that could have utility in many domains. Furthermore, the authors show AnsACR is useable in multiphoton experiments having a peak photocurrent in a commonly used wavelength. Overall, the author's detailed measurements and characterization make for an important resource - both presenting new opsins that may be important for future experiment, and providing characterizations to expand our understanding of opsin biophysics in general.

https://doi.org/10.7554/eLife.106508.2.sa2

Reviewer #3 (Public review):

Summary:

The authors aimed to develop Channelrhodopsins (ChRs), light-gated ion channels, with high potency and blue action spectra for use in multicolor (multiplex) optogenetics applications. To achieve this, they performed a bioinformatics analysis to identify ChR homologues in several protist species, focusing on ChRs from ancyromonads, which exhibited the highest photocurrents and the most blue-shifted action spectra among the tested candidates. Within the ancyromonad clade, the authors identified two new anion-conducting ChRs and one cation-conducting ChR. These were characterized in detail using a combination of manual and automated patch-clamp electrophysiology, absorption spectroscopy, and flash photolysis. The authors also explored sequence features that may explain the blue-shifted action spectra and differences in ion selectivity among closely related ChRs.

Strengths:

A key strength of this study is the high-quality experimental data, which were obtained using well-established techniques such as manual patch-clamp and absorption spectroscopy, complemented by modern automated patch-clamp approaches. These data convincingly support most of the claims. The newly characterized ChRs expand the optogenetics toolkit and will be of significant interest to researchers working with microbial rhodopsins, those developing new optogenetic tools, as well as neuro- and cardioscientists employing optogenetic methods.

Weaknesses:

This study does not exhibit major methodological weaknesses.

https://doi.org/10.7554/eLife.106508.2.sa1

Author response:

> ***Reviewer #1 (Public review):***
>
> *Summary:*
>
> *This work by Govorunova et al. identified three naturally blue-shifted channelrhodopsins (ChRs) from ancyromonads, namely AnsACR, FtACR, and NlCCR. The phylogenetic analysis places the ancyromonad ChRs in a distinct branch, highlighting their unique evolutionary origin and potential for novel applications in optogenetics. Further characterization revealed the spectral sensitivity, ionic selectivity, and kinetics of the newly discovered AnsACR, FtACR, and NlCCR. This study also offers valuable insights into the molecular mechanism underlying the function of these ChRs, including the roles of specific residues in the retinal-binding pocket. Finally, this study validated the functionality of these ChRs in both mouse brain slices (for AnsACR and FtACR) and in vivo in Caenorhabditis elegans (for AnsACR), demonstrating the versatility of these tools across different experimental systems.*
>
> *In summary, this work provides a potentially valuable addition to the optogenetic toolkit by identifying and characterizing novel blue-shifted ChRs with unique properties.*
>
> *Strengths:*
>
> *This study provides a thorough characterization of the biophysical properties of the ChRs and demonstrates the versatility of these tools in different ex vivo and in vivo experimental systems. The mutagenesis experiments also revealed the roles of key residues in the photoactive site that can affect the spectral and kinetic properties of the channel.*

We thank the Reviewer for his/her positive evaluation of our work.

> *Weaknesses:*
>
> *While the novel ChRs identified in this work are spectrally blue-shifted, there still seems to be some spectral overlap with other optogenetic tools. The authors should provide more evidence to support the claim that they can be used for multiplex optogenetics and help potential end-users assess if they can be used together with other commonly applied ChRs. Additionally, further engineering or combination with other tools may be required to achieve truly orthogonal control in multiplexed experiments.*

To demonstrate the usefulness of ancyromonad ChRs for multiplex optogenetics as a proof of principle, we co-expressed AnsACR with the red-shifted cation-conducting ChR Chrimson and measured net photocurrent generated by this combination as a function of the wavelength. We found that it is hyperpolarizing in the blue region of the spectrum, and depolarizing at the red region. In the revision, we added a new panel (Figure 1D) showing these results and the following paragraph to the main text:

"To test the possibility of using AnsACR in multiplex optogenetics, we co-expressed it with the red-shifted CCR Chrimson (Klapoetke et al., 2014) fused to an EYFP tag in HEK293 cells. We measured the action spectrum of the net photocurrents with 4 mM Cl^- in the pipette, matching the conditions in the neuronal cytoplasm (Doyon, Vinay et al. 2016). Figure 1D, black shows that the direction of photocurrents was hyperpolarizing upon illumination with $\lambda<500$ nm and depolarizing at longer wavelengths. A shoulder near 520 nm revealed a FRET contribution from EYFP (Govorunova, Sineshchekov et al. 2020), which was also observed upon expression of the Chrimson construct alone (Figure 1D, red)".

> *In the C. elegans experiments, partial recovery of pharyngeal pumping was observed after prolonged illumination, indicating potential adaptation. This suggests that the effectiveness of these ChRs may be limited by cellular adaptation mechanisms, which could be a drawback in long-term experiments. A thorough discussion of this challenge in the application of optogenetics tools would prove very valuable to the readership.*

We added the following paragraph to the revised Discussion:

"One possible explanation of the partial recovery of pharyngeal pumping that we observed after 15-s illumination, even at the highest tested irradiance, is continued attenuation of photocurrent during prolonged illumination (desensitization). However, the rate of AnsACR desensitization (Figure 1 – figure supplement 4A and Figure 1 – figure supplement 5A) is much faster than the rate of the pumping recovery, reducing the likelihood that desensitization is driving this phenomenon. Another possible reason for the observed adaptation is an increase in the cytoplasmic Cl^- concentration owing to AnsACR activity and hence a breakdown of the Cl^- gradient on the neuronal membrane. The C. elegans pharynx is innervated by 20 neurons, 10 of which are cholinergic (Pereira, Kratsios et al. 2015). A pair of MC neurons is the most important for regulation of pharyngeal pumping, but other pharyngeal cholinergic neurons, including I1, M2, and M4, also play a role (Trojanowski, Padovan-Merhar et al. 2014). Moreover, the pharyngeal muscles generate autonomous contractions in the presence of acetylcholine tonically released from the pharyngeal neurons (Trojanowski, Raizen et al. 2016). Given this complexity, further elucidation of pharyngeal pumping adaptation mechanisms is beyond the scope of this study."

> ***Reviewer #2 (Public review):***
>
> *Summary:*
>
> *Govorunova et al present three new anion opsins that have potential applications in silencing neurons. They identify new opsins by scanning numerous databases for sequence homology to known opsins, focusing on anion opsins. The three opsins identified are uncommonly fast, potent, and are able to silence neuronal activity. The authors characterize numerous parameters of the opsins.*
>
> *Strengths:*
>
> *This paper follows the tradition of the Spudich lab, presenting and rigorously characterizing potentially valuable opsins. Furthermore, they explore several mutations of the identified opsin that may make these opsins even more useful for the broader*

> *community. The opsins AnsACR and FtACR are particularly notable, having extraordinarily fast onset kinetics that could have utility in many domains. Furthermore, the authors show that AnsACR is usable in multiphoton experiments having a peak photocurrent in a commonly used wavelength. Overall, the author's detailed measurements and characterization make for an important resource, both presenting new opsins that may be important for future experiments, and providing characterizations to expand our understanding of opsin biophysics in general.*

We thank the Reviewer for his/her positive evaluation of our work.

> *Weaknesses:*
>
> *First, while the authors frequently reference GtACR1, a well-used anion opsin, there is no side-by-side data comparing these new opsins to the existing state-of-the-art. Such comparisons are very useful to adopt new opsins.*

GtACR1 exhibits the peak sensitivity at 515 nm and therefore is poorly suited for combination with red-shifted CCRs or fluorescent sensors, unlike blue-light-absorbing ancyromonad ACRs. Nevertheless, we conducted side-by-side comparison of ancyromonad ChRs, GtACR1 and GtACR2, the latter of which has the spectral maximum at 470 nm. The results are shown in the new Figures 1E and F, and the new multipanel Figure 1 – figure supplement 4 added in the revision. We also added the following text, describing these results, to the revised Results section:

“Figures 1E and F show the dependence of the peak photocurrent amplitude and reciprocal peak time, respectively, on the photon flux density for ancyromonad ChRs and GtACRs. The current amplitude saturated earlier than the time-to-peak for all tested ChRs. Figure 1 – figure supplement 4A-E shows normalized photocurrent traces recorded at different photon densities. Quantitation of desensitization at the end of 1-s illumination revealed a complex light dependence (Figure 1, Figure Supplement 4F). Figure 1 – figure supplement 5 shows normalized photocurrent traces recorded in response to a 5-s light pulse of the maximal available intensity and the magnitude of desensitization at its end.”

> *Next, multiphoton optogenetics is a promising emerging field in neuroscience, and I appreciate that the authors began to evaluate this approach with these opsins. However, a few additional comparisons are needed to establish the user viability of this approach, principally the photocurrent evoked using the 2p process, for given power densities. Comparison across the presented opsins and GtACR1 would allow readers to asses if these opsins are meaningfully activated by 2P.*

We carried out additional 2P experiments in ancyromonad ChRs, GtACR1 and GtACR2 and added their results to a new main-text Figure 6 and Figure 6 – figure supplement 1. We added the new section describing these results, “Two-photon excitation”, to the main text in the revision:

“To determine the 2P activation range of AnsACR, FtACR, and NlCCR, we conducted raster scanning using a conventional 2P laser, varying the excitation wavelength between 800 and 1,080 nm (Figure 6 – figure supplement 1). All three ChRs generated detectable photocurrents with action spectra showing maximal responses at ~925 nm for AnsACR, 945 nm for FtACR, and 890 nm for NlCCR (Figure 6A). These wavelengths fall within the excitation range of common Ti:Sapphire lasers, which are widely used in neuroscience laboratories and can be tuned between ~700 nm and 1,020-1,300 nm. To assess desensitization, cells expressing AnsACR, FtACR, or NlCCR were illuminated at the respective peak wavelength of each ChR at 15 mW for 5 seconds. GtACR1 and GtACR2, previously used in 2P experiments (Forli, Vecchia et al. 2018, Mardinly, Oldenburg et al. 2018), were included for comparison. The normalized

photocurrent traces recorded under these conditions are shown in Figure 6B-F. The absolute amplitudes of 2P photocurrents at the peak time and at the end of illumination are shown in Figure 6G and H, respectively. All five tested variants exhibited comparable levels of desensitization at the end of illumination (Figure 6I)."

> ***Reviewer #3 (Public review):***
>
> *Summary:*
>
> *The authors aimed to develop Channelrhodopsins (ChRs), light-gated ion channels, with high potency and blue action spectra for use in multicolor (multiplex) optogenetics applications. To achieve this, they performed a bioinformatics analysis to identify ChR homologues in several protist species, focusing on ChRs from ancyromonads, which exhibited the highest photocurrents and the most blue-shifted action spectra among the tested candidates. Within the ancyromonad clade, the authors identified two new anion-conducting ChRs and one cation-conducting ChR. These were characterized in detail using a combination of manual and automated patch-clamp electrophysiology, absorption spectroscopy, and flash photolysis. The authors also explored sequence features that may explain the blue-shifted action spectra and differences in ion selectivity among closely related ChRs.*
>
> *Strengths:*
>
> *A key strength of this study is the high-quality experimental data, which were obtained using well-established techniques such as manual patch-clamp and absorption spectroscopy, complemented by modern automated patch-clamp approaches. These data convincingly support most of the claims. The newly characterized ChRs expand the optogenetics toolkit and will be of significant interest to researchers working with microbial rhodopsins, those developing new optogenetic tools, as well as neuro- and cardioscientists employing optogenetic methods.*

We thank the Reviewer for his/her positive evaluation of our work.

> *Weaknesses:*
>
> *This study does not exhibit major methodological weaknesses. The primary limitation of the study is that it includes only a limited number of comparisons to known ChRs, which makes it difficult to assess whether these newly discovered tools offer significant advantages over currently available options.*

We conducted side-by-side comparison of ancyromonad ChRs and GtACRs, wildly used for optical inhibition of neuronal activity. The results are shown in the new Figures 1E and F, and the new multipanel Figure 1 – figure supplement 4 and Figure 1 – figure supplement 5 added in the revision. We also added the following text, describing these results, to the revised Results section:

"Figures 1E and F show the dependence of the peak photocurrent amplitude and reciprocal peak time, respectively, on the photon flux density for ancyromonad ChRs and GtACRs. The current amplitude saturated earlier than the time-to-peak for all tested ChRs. Figure 1 – figure supplement 4A-E shows normalized photocurrent traces recorded at different photon densities. Quantitation of desensitization at the end of 1-s illumination revealed a complex light dependence (Figure 1, Figure Supplement 4F). Figure 1 – figure supplement 5 shows normalized photocurrent traces recorded in response to a 5-s light pulse of the maximal available intensity and the magnitude of desensitization at its end."

> *Additionally, although the study aims to present ChRs suitable for multiplex optogenetics, the new ChRs were not tested in combination with other tools. A key requirement for multiplexed applications is not just spectral separation of the blue-shifted ChR from the red-shifted tool of interest but also sufficient sensitivity and potency under low blue-light conditions to avoid cross-activation of the respective red-shifted tool. Future work directly comparing these new ChRs with existing tools in optogenetic applications and further evaluating their multiplexing potential would help clarify their impact.*

As a proof of principle, we co-expressed AnsACR with the red-shifted cation-conducting CCR Chrimson and demonstrated that the net photocurrent generated by this combination is hyperpolarizing in the blue region of the spectrum, and depolarizing at the red region. In the revision, we added a new panel (Figure 1D) showing these results and the following paragraph to the main text:

"To test the possibility of using AnsACR in multiplex optogenetics, we co-expressed it with the red-shifted CCR Chrimson (Klapoetke et al., 2014) fused to an EYFP tag in HEK293 cells. We measured the action spectrum of the net photocurrents with 4 mM Cl^- in the pipette, matching the conditions in the neuronal cytoplasm (Doyon, Vinay et al. 2016). Figure 1D, black shows that the direction of photocurrents was hyperpolarizing upon illumination with $\lambda<500$ nm and depolarizing at longer wavelengths. A shoulder near 520 nm revealed a FRET contribution from EYFP (Govorunova, Sineshchekov et al. 2020), which was also observed upon expression of the Chrimson construct alone (Figure 1D, red)".

> ***Reviewing Editor Comments:***
>
> *The reviewers suggest that direct comparison to GtACR1 is the most important step to make this work more useful to the community.*

We followed the Reviewers' recommendations and carried out side-by-side comparison of ancyromonad ChRs and GtACR1 as well as GtACR2 (Figure 1E and F, Figure 1 – figure supplement 4, Figure 1 – figure supplement 5, and Figure 6). Note, however, that GtACR1's spectral maximum is at 515 nm, which makes it poorly suitable for blue light excitation. Also, ChRs are known to perform very differently in different cell types and upon expression of their genes in different vector backbones, so our results cannot be generalized for all experimental systems. Each ChR user needs to select the most appropriate tool for his/her purpose by testing several candidates in his/her own experimental setting.

> ***Reviewer #1 (Recommendations for the authors):***
>
> *(1) The figure legend for Figure 2D-I appears to be incomplete. Please provide a detailed explanation of the panels.*

In the revision, we have expanded the legend of Figure 2 to explain all individual panels.

> *(2) The meaning of the Vr shift (Y-axis in Figure 2H-I) should be clarified in the main text to aid reader understanding.*

In the revision, we added the phrase "which indicated higher relative permeability to NO_3 than to Cl^-" to explain the meaning of the Vr shift upon replacement of Cl^- with NO_3-.

> *(3) Adding statistical analysis for the peak and end photocurrent values in Figure 2D-F would strengthen the claim that there is minimal change in relative permeability during illumination.*

In the revision, we added the V_r values for the peak photocurrent to Figure 2H-I, which already contained the V_r values for the end photocurrent, and carried out a statistical analysis of their comparison. The following sentence was added to the text in the revision:

"The V_r values of the peak current and that at the end of illumination were not significantly different by the two-tailed Wilcoxon signed-rank test (Fig. 2G), indicating no change in the relative permeability during illumination."

> *(4) Figure 4H and I seem out of place in Figure 4, as the title suggests a focus on wild-proteins and AnsACR mutants. The authors could consider moving these panels to Figure 3 for better alignment with the content.*

As noted below, we changed the panel order in Figure 4 upon the Reviewer's request. In particular, former Figure 4I is Figure 4C in the revision, and former Figure 4H is now panel C in Figure 3 – figure supplement 1 in the revision. We rearranged the corresponding section of the text (highlighted yellow in the manuscript).

> *(5) The characterization section could be strengthened by including data on the pH sensitivity of FtACR, which is currently missing from the main figures.*

Upon the Reviewer's request, we carried out pH titration of FtACR absorbance and added the results as Figure 4B in the revision.

> *(6) The logic in Figure 4A-G appears somewhat disjointed. For example, Figure 4A shows pH sensitivity for WT AnsACR and the G86E mutant, while Figure 4 B-D shifts to WT AnsACR and the D226N mutant, and Figure 4E returns to the G86E mutant. Reorganizing or clarifying the flow would improve readability.*

We followed the Reviewer's advice and changed the panel order in Figure 4. In the revised version, the upper row (panels A-C) shows the pH titration data of the three WTs, the middle row (panels D-F) shows analysis of the AnsACR_D226N mutant, and the lower row (panels G-I) shows analysis of the AnsACR_G88E mutant. We also rearranged accordingly the description of these panels in the text.

> *(7) In Figure 5A, "NIACR" should likely be corrected to "NlCCR".*

We corrected the typo in the revision.

> *(8) The statistical significance in Figure 6C and D is somewhat confusing. Clarifying which groups are being compared and using consistent symbols would improve interoperability.*

In the revision, we improved the figure panels and legend to clarify that the comparisons are between the dark and light stimulation groups within the same current injection.

> *(9) The authors pointed out that at rest or when a small negative current was injected, the neurons expressing Cl- permeable ChRs could generate a single action potential at the beginning of photostimulation, as has been reported before. The authors could help by further discussing if and how this phenomenon would affect the applicability of such tools.*

We mentioned in the revised Discussion section that activation of ACRs in the axons could depolarize the axons and trigger synaptic transmission at the onset of light stimulation, and this undesired excitatory effect need to be taken into consideration when using ACRs.

> ***Reviewer #2 (Recommendations for the authors):***
>
> *Govorunova et al present three new anion opsins that have potential applications in silencing neurons. This paper follows the tradition of the Spudich lab, presenting and rigorously characterizing potentially valuable opsins. Furthermore, they explore several mutations of the identified opsin that may make these opsins even more useful for the broader community. In general, I feel positively about this manuscript. It presents new potentially useful opsins and provides characterization that would enable its use. I have a few recommendations below, mostly centered around side-by-side comparisons to existing opsins.*
>
> *(1) My primary concern is that while there is a reference to GtACR1, a highly used opsin first described by this team, they do not present any of this data side by side.*
>
> *When evaluating opsins to use, it is important to compare them to the existing state of the art. As a potential user, I need to know where these opsins differ. Citing other papers does not solve this as, even within the same lab, subtle methodological differences or data plotting decisions can obscure important differences.*

As we explained in the response to the public comments, we carried out side-by-side comparison of ancyromonad ChRs and GtACRs as requested by the Reviewer. The results are shown in the new Figures 1E and F, and the new multipanel Figure 1 – figure supplement 4 and Figure 1 – figure supplement 5, added in the revision. However, we would like to emphasize a limited usefulness of such comparative analysis, as ChRs are known to perform very differently in different cell types and upon expression of their genes in different vector backbones, so our results cannot be generalized for all experimental systems. Each ChR user needs to select the most appropriate tool for his/her purpose by testing several candidates in his/her own experimental setting.

> *(2) Multiphoton optogenetics is an emerging field of optogenetics, and it is admirable that the authors address it here. The authors should present more 2p characterization, so that it can be established if these new opsins are viable for use with 2P methods, the way GtACR1 is. The following would be very useful for 2P characterization:*
>
> *Photocurrents for a given power density, compared to GtACR1 and GtACR2.*

The new Figure 6 (B-F) added in the revision shows photocurrent traces recorded from the three ancyromonad ChRs and two GtACRs upon 2P excitation of a given power density.

> *Comparing NICCR and FtACR's wavelength specificity and photocurrent. If these opsins are too weak to create reasonable 2P spectra, this difference should be discussed.*

The new Figure 6A shows the 2P action spectra of all three ancyromonad ChRs.

> *A Trace and calculated photocurrent kinetics to compare 1P and 2P. This need not be the flash-based absorption characterization of Figure 3, but a side-by-side photocurrent as in Figure 2.*

As mentioned above, photocurrent traces recorded from ancyromonad ChRs and GtACRs upon 2P excitation are shown in the new Figure 6 (B-F). However, direct comparison of the 2P data with the 1P data is not possible, as we used laser scanning illumination for the former and wild-field illumination for the latter.

> *Characterization of desensitization. As the authors mention, many opsins undergo desensitization, presenting the ratio of peak photocurrent vs that at multiple time points (probably up to a few seconds) would provide evidence for how effectively these constructs could be used in different scenarios.*
>
> *We conducted a detailed analysis of desensitization under both 1P and 2P excitation. The new Figure 1 – figure supplement 4 and Figure 1 – figure supplement 5 show the data obtained under 1P excitation, and the new Figure 6 shows the data for 2P conditions.*
>
> *I have to admit, that by the end of the paper, I was getting confused as to which of the three original constructs had which property, and how that was changing with each mutation. I would suggest that a table summarizing each opsin and mutation with its onset and offset kinetics, peak wavelength, photocurrent, and ion selectivity would greatly increase the ability to select and use opsins in the future.*

In the revision, we added a table of the spectroscopic properties of all tested mutants as Supplementary File 2. This study did not aim to analyze other parameters listed by the Reviewer. We added the following sentence referring to this table to the main text:

“Supplementary File 2 contains the λ values of the half-maximal amplitude of the long-wavelength slope of the spectrum, which can be estimated more accurately from the action spectra than the λ of the maximum.”

> *It may be out of the scope of this manuscript, but if a soma localization sequence can be shown to remove the 'axonal spiking' (as described in line 441), this would be a significant addition to the paper.*

Our previous study (Messier et al., 2018, doi: 10.7554/eLife.38506) showed that a soma localization sequence can reduce, but not eliminate, the axonal spiking. We plan to test these new ACRs with the trafficking motifs in the future.

> *NICCR appears to have the best photocurrents of all tested opsins in this paper. It seems odd that it was omitted from the mouse cortical neurons experiments.*

We have not included analysis of NlCCR behavior in neurons because we are preparing a separate manuscript on this ChR.

> *Figure 6 would benefit from more gradation in the light powers used to silence and would benefit from comparison to GtACR. I suggest using a fixed current with a series of illumination intensities to see which of the three opsins (or GtACR) is most effective at silencing. At present, it looks binary, and a user cannot evaluate if any of these opsins would be better than what is already available.*

In the revision, we added the data comparing the light sensitivity of AnsACR and FtACR with previously identified GtACR1 and GtACR2 (new Figure 1E and F) to help users compare these ACRs. Although they are less sensitive to light comparing to GtACR1 and GtACR2, they could still be activated by commercially available light sources if the expression levels are similar. Less sensitive ACRs may have less unwanted activation when using with other optogenetic tools.

> ***Reviewer #3 (Recommendations for the authors):***
>
> *Suggested Improvements to Experiments, Data, or Analyses:*

> *(1) Line 25: "significantly exceeding those by previously known tools" and Line 408: "NlCCR is the most blue-shifted among ancyromonad ChRs and generates larger photocurrents than the earlier known CCRs with a similar absorption maximum." As noted in the public review, this statement applies only to a very specific subgroup of ChRs with spectral maxima below 450 nm. If the goal was to claim that NlCCR is a superior tool among a broader range of blue-light-activated ChRs, direct comparisons with state-of-the-art ChRs such as ChR2 T159C (Berndt et al., 2011), CatCh (Kleinlogel et al., 2014), CoChR (Klapoetke et al., 2014), CoChR-3M (Ganjawala et al., 2019), or XXM 2.0 (Ding et al., 2022) would be beneficial. If the goal was to demonstrate superiority among tools with spectra below 450 nm, I suggest explicitly stating this in the paper.*

The Reviewer correctly inferred that we emphasized the superiority of NlCCR among tools with similar spectral maxima, not all blue-light-activated ChRs available for neuronal photoexcitation, most of which exhibit absorption maxima at longer wavelengths. To clarify this, we added “with similar spectral maxima” to the sentence in the original Line 25. The sentence in Line 408 already contains this clarification: “with a similar absorption maximum”.

> *(2) Lines 111-113: "The absorption spectra of the purified proteins were slightly blue-shifted from the respective photocurrent action spectra (Figure 1D), likely due to the presence of non-electrogenic cis-retinal-bound forms." I would be skeptical of this statement. The spectral shifts in NlCCR and AnsACR are small and may fall within the range of experimental error. The shift in FtACR is more apparent; however, if two forms coexist in purified protein, this should be reflected as two Gaussian peaks in the absorption spectrum (or at least as a broader total peak reflecting two states with close maxima and similar populations). On the contrary, the action spectrum appears to have two peaks, one potentially below 465 nm. Generally, neither spectrum appears significantly broader than a typical microbial rhodopsin spectrum. This question could be clarified by quantifying the widths of the absorption and action spectra or by overlaying them on the same axis. In my opinion, the two spectra seem very similar, and just appearance of the "bump" in the action spectum shifts the apparent maximum of the action spectrum to the red. If there were two states, then they should both be electrogenic, and the slight difference in spectra might be explained by something else (e.g. by a slight difference in the quantum yields of the two states).*

As the Reviewer suggested, in the revision we added a new figure (Figure 1 – figure supplement 2), showing the overlay of the absorption and action spectra of each ancyromonad ChR. This figure shows that the absorption spectra are wider than the action spectra (especially in AnsACR and FtACR), which confirms our interpretation (contribution of the non-electrogenic blue-shifted cis-retinal-bound forms to the absorption spectrum). Note that the presence of such forms explaining a blue shift of the absorption spectrum has been experimentally verified in HcKCR1 (doi: 10.1016/j.cell.2023.08.009; 10.1038/s41467-025-56491-9). Therefore, we revised the text as follows:

“The absorption spectra of the purified proteins (Figure 1C) were slightly blue-shifted from the respective photocurrent action spectra (Figure 1 – figure supplement 3), likely due to the presence of non-electrogenic cis-retinal-bound forms. The presence of such forms, explaining the discrepancy between the absorption and the action spectra, was verified by HPLC in KCRs (Tajima et al. 2023, Morizumi et al., 2025).”

> *(3) Lines 135-136: "The SyncroPatch enables unbiased estimation of the photocurrent amplitude because the cells are drawn into the wells without considering their tag fluorescence." While SyncroPatch does allow unbiased selection of patched cells, it does not account for the fraction of transfected cells. Without a method to exclude non-*

> *transfected cells, which are always present in transient transfections, the comparison of photocurrents may be affected by the proportion of untransfected cells, which could vary between constructs. To clarify whether the statistically significant difference in the Kolmogorov-Smirnov test could indicate that the fraction of transfected cells after 48-72h differs between constructs, I suggest analyzing only transfected cells or reporting fractions of transfected cells by each construct.*

The Reviewer correctly states that non-transfected cells are always present in transiently transfected cell populations. However, his/her suggestion to “exclude non-transfected cells” is not feasible in the absence of a criterion for such exclusion. As it is evident from our data, transient transfection results in a continuum of the amplitude values, and it is not possible to distinguish a small photocurrent from no photocurrent, considering the noise level. We would like, however, to emphasize that not excluding any cells provides an estimate of the overall potency of each ChR variant, which depends on both the fraction of transfected cells and their photocurrents. This approach mimics the conditions of in vivo experiments, when non-expressing cells also cannot be excluded.

> *(4) Line 176: "AnsACR and FtACR photocurrents exhibited biphasic rise." The fastest characteristic time is very close to the typical resolution of a patch-clamp experiment (RC = 50 μs for a 10 pF cell with a 5 MΩ series resistance). Thus, I am skeptical that the faster time constant of the biphasic opening represents a protein-specific characteristic time. It may not be fully resolved by patch-clamp and could simply result from low-pass filtering of a specific cell. I suggest clarifying this for the reader.*

The Reviewer is right that the patch clamp setup acts as a lowpass filter. Earlier, we directly measured its time resolution (~15 μs) by recording the ultrafast (occurring on the ps time scale) charge movements related to the trans-cis isomerization (doi: 10.1111/php.12558). However, the lowpass filter of the setup can only slow the entire signal, but cannot lead to the appearance of a separate kinetic component (i.e. a monophasic process cannot become biphasic). Therefore, we believe that the biphasic photocurrent rise reflects biphasic channel opening rather than a measurement artifact. Two phases in the channel opening have also been detected in GtACR1 (doi: 10.1073/pnas.1513602112) and CrChR2 (10.1073/pnas.1818707116).

> *(5) Line 516: "The forward LED current was 900 mA." It would be more informative to report the light intensity rather than the forward current, as many readers may not be familiar with the specific light output of the used LED modules at this forward current.*

We have added the light intensity value in the revision:

“The forward LED current was 900 mA (which corresponded to the irradiance of ~2 mW mm^{-2})…”

> *(6) Lines 402-403: "The NlCCR … contains a neutral residue in the counterion position (Asp85 in BR), which is typical of all ACRs. Yet, NlCCR does not conduct anions, instead showing permeability to Na+." This is not atypical for CCRs and has been demonstrated in previous works of the authors (CtCCR in Govorunova et al. 2021, ChvCCR1 in Govorunova et al. 2022). What is unique is the absence of negatively charged residues in TM2, as noted later in the current study. However, the absence of negatively charged residues in TM2 appears to be rare for ACRs as well. Not as a strong point of criticism, but to enhance clarity, I suggest analyzing the frequency of carboxylate residues in TM2 of ACRs to determine whether the unique finding is relevant to ion selectivity or to another property.*

The Reviewer is correct that some CCRs lack a carboxylate residue in the D85 position, so this feature alone cannot be considered as a differentiating criterion. However, the complete absence of glutamates in TM2 is not rare in ACRs and is found, for example, in HfACR1 and CarACR2. We have discussed this issue in our earlier review (doi: 10.3389/fncel.2021.800313) and do not think that repeating this discussion in this manuscript is appropriate.

> ***Recommendations for Writing and Presentation:***
>
> *(1) Some figures contain incomplete or missing labels:*
>
> *Figure 2: Panels D to I lack labels.*

In the revision, we have expanded the legend of Figure 2 to explain all individual panels.

> *Figure 3 - Figure Supplement 1: Missing explanations for each panel.*

In the revision, we changed the order of panes and explained all individual panels in the legend.

> *Figure 5 - Figure Supplement 1: Missing explanations for each panel.*

No further explanation for individual panels in this Figure is needed because all panels show the action spectra of various mutants, the names of which are provided in the panels themselves. Repeating this information in the figure legend would be redundant.

> *(2) In Figure 2, "sem" is written in lowercase, whereas "SEM" is capitalized in other figures. Standardizing the format would improve consistency.*

In the revision, we changed the font of the SEM abbreviation to the uppercase in all instances.

> *(3) Line 20: "spectrally separated molecules must be found in nature." There is no proof that they cannot be developed synthetically; rather, it is just difficult. I suggest softening this statement, as the findings of this study, together with others, will probably allow designing molecules with specified spectral properties in the future.*

In the revision, we changed the cited sentence to the following:

“Multiplex optogenetic applications require spectrally separated molecules, which are difficult to engineer without disrupting channel function”.

> *(4) Line 216-219: "Acidification increased the amplitude of the fast current ~10-fold (Figure 4F) and shifted its Vr ~100 mV (Figure 3 - figure supplement 1D), as expected of passive proton transport. The number of charges transferred during the fast peak current was >2,000 times smaller than during the channel opening, from which we concluded that the fast current reflects the movement of the RSB proton." The claim about passive transport of the RSB proton should be clarified, as typically, passive transport is not limited to exactly one proton per photocycle, and the authors observe the increase in the fast photocurrents upon acidification.*

We thank the Reviewer for pointing out the confusing character of our description. To clarify the matter, we added a new photocurrent trace to Figure 4I in the revision recorded from AnsACR_G86E at 0 mV and pH 7.4. We have rewritten the corresponding section of Results as follows:

"Its rise and decay τ corresponded to the rise and decay τ of the fast positive current recorded from AnsACR_G86E at 0 mV and neutral pH, superimposed on the fast negative current reflecting the chromophore isomerization (Figure 4I, upper black trace). We interpret this positive current as an intramolecular proton transfer to the mutagenetically introduced primary acceptor (Glu86), which was suppressed by negative voltage (Figure 4I, lower black trace). Acidification increased the amplitude of the fast negative current ~10-fold (Figure 4I, black arrow) and shifted its V_r ~100 mV to more depolarized values (Figure 4 – figure supplement 2A). This can be explained by passive inward movement of the RSB proton along the large electrochemical gradient."

> *Minor Corrections:*
>
> *(1) Line 204: Missing bracket in "phases in the WT (Figure 4D."*

The quoted sentence was deleted during the revision.

> *(2) Line 288: Typo-"This Ala is conserved" should probably be "This Met is conserved."*

We mean here the Ala four residues downstream from the first Ala. To avoid confusion, we changed the cited sentence to the following:

"The Ala corresponding to BR's Gly122 is also found in AnsACR and NlCCR (Figure 5A)…"

> *(3) Lines 702-704: Missing Addgene plasmid IDs in "(plasmids #XXX and #YYY, respectively)."*

In the revision, we added the missing plasmid IDs.

https://doi.org/10.7554/eLife.106508.2.sa0